A Study of Impurity State and its Implication in Inorganic and Organic Semiconductors

Chi-Ken Lu

Institute of Physics
National Chiao Tung University

Advisor: Prof. Hsin-Fei Meng

Abstract

In this thesis we deal with a few problems related to the presence of impurity in semiconductors. The focus of Part I is on the realization of THz radiation in solid state system by using the concept of resonant state, a hybrid state of localized impurity state and a band of continuum. The previous proposal on such resonant state laser, however, has a serious constrain on the applied strain, and consequently the emitted photon has a lower bound of energy. We invent a quantum well structure in order to relax such constrain and generate photon of energy less than 4 meV, corresponding to frequency of 1 THz, with feasible conditions of strain, impurity concentration, electric field, and temperature. We demonstrate that a population inversion can be achieved in this structure by numerically solving the Boltzmann kinetic equation in momentum space.

Part II is devoted to the investigation of the effects of oxygen adsorption on the electronic properties of conjugated polymers. It is found that the oxygen molecule has the tendency to adsorb onto the category of carbon-based materials with sp^2-binding, such as carbon nanotube and most of the conjugated polymers, by a weak intermolecular interaction. There are two outstanding questions regarding such adsorption. One of them is the huge mobility difference between hole and electron in many conjugated polymers. This is in contrast to the situation for the crystalline inorganic solids in which the electrons have a larger mobility than the holes. The simple formula for the carrier mobility in terms of effective mass and scattering time is apparently invalid to explain such imbalance in such disorder system because accurate band structure calculation reveals two similar effective masses for conduction and valence bands. Therefore it is the presence of defect that dominate the transport in such disorder system, and hence the observed mobility is influenced by the trap density to a great extent. The ultimate entity for such imbalance is shown to be the adsorbed oxygen molecule which causes a pair of asymmetric binding energies for the trapped electron and hole in a symmetric electronic system.

P-doping by the adsorbed gas molecule is another interesting property of conjugated polymers. A reversible increase of conductivity is found in the polymer FET when the polymer was previously exposed to air for a few hours. The increase of conductivity, however, causes the degrade of the device characteristics by increasing the off-current. This effect can be completely eliminated by just evacuating the devices for a long time, say a week. The doping mechanism remains unclear because of the conditional illumination.

For polythiophene, the doping can be found in both dark and illumination, while it is only possible under illumination for pentacene. We would like to understand the mechanism for such doping process. Polythiophene is taken as an example by calculating the band structure for the oxygenated polythiophene with a self-consistent tight-binding scheme. The coincidence of Fermi level and the valence band edge reveals that a cluster of adsorbed oxygen molecules transform the semiconducting polymers into metal. Such coincidence is shown to depend on the HOMO level of the host. In addition, an excitation corresponding to electron transferring to the adsorbate is also found in the band structure. The metal-insulator transition explains the doping in dark and the charge transfer excitation is interpreted as the photoinduced doping.

Contents

Part I

Realization of THz radiation in solid state system

Chapter 1

Overview of solid-state THz source

1.1 Introduction

Applications of electromagnetic radiation are ubiquitous in our daily lives from personal communications, microwave ovens, to X-ray in medical detections. For scientific studies, those radiations can be used to unravel the underlying structures of tiny objects ranging from the elementary atoms, molecules, to tissues. THz radiation, whose frequency ($1-10$ THz) falling in the range between infrared and microwave regions of the spectrum, has a wavelength ($30-300$ μm) comparable to the size of human tissues and hence it is very desirable for medical imaging such as detecting cancers or other diseases. Despite of the wide applications, THz frequencies are among the least developed electromagnetic spectra. The underdevelopment is primarily due to lack of convenient THz sources that can provide high radiation intensities with cw operation. Radiation sources based on solid state media are thus highly desirable due to its size and the potential integration with other electronic applications. However, it is difficult to achieve the population inversion conditions for this range of frequency in solid state system because some thermal processes, like acoustic phonon scattering and Auger relaxation, inherent for solids have energy scale of meV, and hence can equalize non-equilibrium carrier distributions of states spaced by a few THz.

Since the original proposal of semiconductor superlattices, there has been much progress to obtain optical gain in such novel system. In this chapter we are going to review three different schemes to generate THz radiation based on the solid state quantum structures. For quantum cascade laser and resonant state laser, a population inversion between levels where transition

4
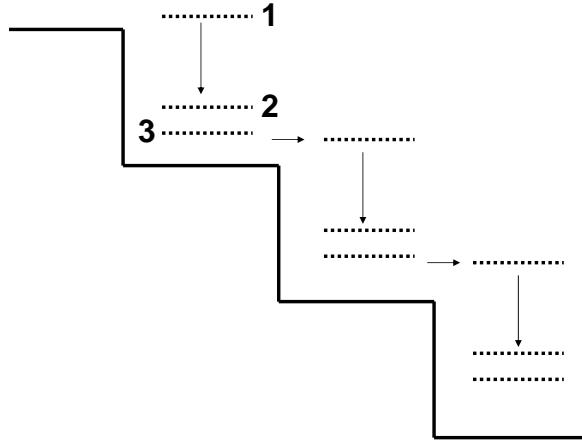
Figure 1.1: A schematic plot for quantum cascade laser. As shown, the carriers injected from the left tunnel into the state **1** and followed by a slow decay to state **2**. With precise control of the barrier height and well width, state **2** can fast decay into state **3**, which in turn depopulates state **2**. A population inversion is then achieved when the decay from **1** to **2** is slow. Identical process takes place in the next block.

takes place is the key ingredient to obtain light amplification. However, the emission of THz radiation resulting from Bloch oscillation still can have optical gain without population inversion. Among these, the focus is on the resonant state laser which use a hybridized state of a localized impurity state and the continuous valence band states. Motivated by the constrain on the energy of emitted photon in previous proposals, we invent a new quantum well structure to implement such concept but free of such constrain. The details of lasing mechanism and the theoretical analysis will be given in the following chapters.

1.2   Quantum cascade laser

The quests for solid state radiation sources usually rely on precise manipulation of carrier's kinetics such that the optical gain can be obtained between levels of transition. In other words, a population inversion is necessary for the lasing condition. The usual and convenient external forces which drive

the distribution deviating from the its equilibrium one is electric field. The energy difference for carrier transition in THz frequencies has the order of meV, which is much smaller than the band gap, usually of order eV, in most semiconductors. Thus the transition must take place within a single band. This is possible when considering the subband structure brought by the fancy structure like quantum well or super lattice.

Fig. 1.1 shows a schematic plot for the operation of quantum cascade laser. The relevant levels in a principal block are labeled by **1**, **2** and **3**. The actual device contains a few periods of such block. Usually the carriers are injected by resonant tunneling. By precise control of width of quantum wells and the the barriers, state **1** can have a relatively slow decay into state **2** by localizing the wave function for state **1**. The depopulation of state **2** can be achieved by the fast decay from **2** to **3**. A new cycle starts when carriers from **3** tunnel into state **1** in the next block. Fig. 1.2 shows the potential profile in an actual quantum cascade laser based on Si/SiGe superlattices where the THz radiations result from intersubband electroluminescence[1]. In addition it has been demonstrated to emit cw radiation of 3.2 THz at liquid-nitrogen temperature in GaAs/AlGaAs SLs[2].

However, building QCLs at such long wavelengths becomes increasingly challenging since the intersubband energy separations are extremely small (1 THz corresponds to 4 meV). It becomes difficult to achieve the selective injection and removal of carriers necessary to obtain an intersubband population inversion, especially as the energy separations become comparable to the subband broadenings. Furthermore, the free carrier absorption loss scales as λ^2 and thus increases significantly at low frequencies[3]. To date the design based on QCL is able to emit radiation of 1 THz.[4]

1.3   Bloch oscillation

The dynamics of a electron moving freely in a perfectly periodic potential under an applied constant electric field is simple. If we approximate the band dispersion as

$$\varepsilon = \frac{\Delta}{2}(1 - \cos kd) \,, \tag{1.1}$$

then the velocity of the electron can be expressed as

$$v(k) = \frac{1}{\hbar}\frac{\partial \varepsilon}{\partial k} = \frac{\Delta d}{2\hbar} \sin kd \,, \tag{1.2}$$

where the momentum is a function of the applied electric field, given by
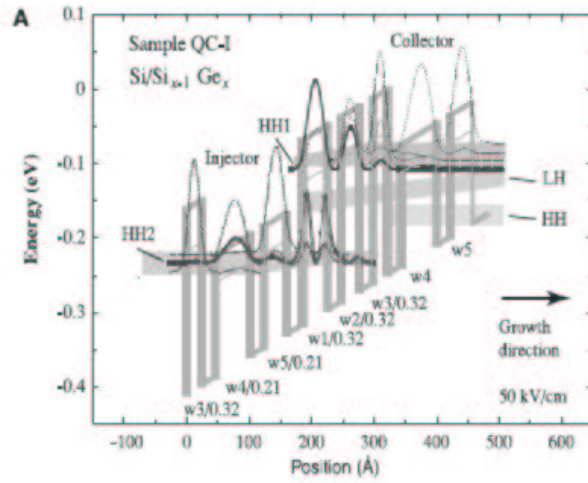
Figure 1.2: The valence band potential for a quantum cascade laser in Si/SiGe superlattice[1]. With precise control of the well widths and the Ge content, two series of states, labeled by HH1 and HH2, are separated by a gap of 130 meV and a transition takes place between them. When a DC electric field is applied, holes on HH2 states can easily arrive at w1 by tunneling but is quenched there due to small overlap between wave functions for HH1 and HH2. The quench therefore generates a sufficiently long life time for HH2, and a population inversion is possible when more and more holes are injected. This block is repeated for a few cycles in the real device.

$$k(t) = k_0 + \frac{eEt}{\hbar} \ . \tag{1.3}$$

Thus the electron has a sinusoid velocity under the constant electric field. That is

$$v(t) = \frac{\Delta d}{2\hbar} \sin(\omega_B t) \ , \tag{1.4}$$

where ω_B is the Bloch oscillation frequency

$$\omega_B = \frac{eEd}{\hbar} \ . \tag{1.5}$$

Therefore, the electron can move back and forth in both real and momentum spaces for such ideal situation[5, 6]. The spatial amplitude for Bloch oscillation is about Δ/eE. For real situation when electric field of order kV/cm and bandwidth Δ of order eV, this amplitude is much larger than the lattice constant, which suggests that such oscillation is not possible to be observed at room temperature. However, in the structure of superlattice, this amplitude can be significantly reduced since the subband has much smaller Δ. In addition, the frequency ω_B can be fine tuned to match THz range by adjusting the layer spacing and the applied field. Key experiments in semiconductor superlattices have shown Wannier-Stark ladders, transient Bloch oscillations, and resonant THz photoconductivity[7, 8, 9].

1.4   Strain-induced resonant state laser

Another promising way to realize semiconductor source of THz radiation is resonant state lasers[10, 11] (RSL) based on doped quantum well (QW) structures,[12, 13] whose operation involves strain-induced resonant states and pumping by an electric field. A THz transition between higher and lower acceptor states has been observed.[12, 13] In RSL with one single QW, the two degenerate valence bands are split by symmetry-lowering external strain caused by external pressure or lattice mismatch. The splitting also removes the degeneracy of the hydrogen-like acceptor localized states and therefore two localized states are formed with energy levels attached to each split band. As the strain is so strong that the energy splitting exceeds the binding energy of the acceptor, one of the two localized states becomes resonant with the band to which the other localized state is attached. The coincidence in energy leads to resonant scattering between the continuous and localized states. A population inversion between the two localized states can be achieved by resonant capture of the holes under an electric field.
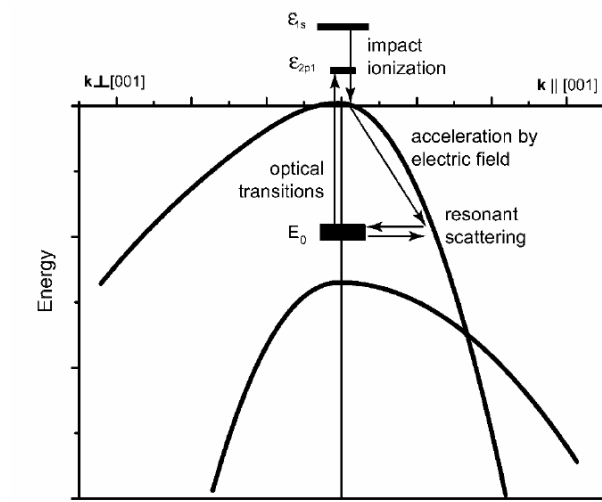
Figure 1.3: A schematic of the operation for emission of THz radiation based on the resonant state in strained p-Ge[11]. As shown, the resonant state is a combination of the valence band continuum and the localized acceptor state. The hybridization is through an off-diagonal coupling between states of different j_z.

Shown in Fig. 1.3 is the valence band diagram for the strained semiconductor as well as a series of acceptor states attached to them. The split between the two bands is proportional to the strain. Therefore the acceptor state, labeled by the thick line, can have a energy resonance with the continuum. Though the localized state and the continuum have different angular momentum component j_z, they can form a resonant state by coupling with each other through an small off-diagonal interaction in the Luttinger Hamiltonian[11]. In thermal equilibrium the lowest for hole carrier is the acceptor 1s state shown in the top of Fig. 1.3. Therefore at very low temperature all the holes occupy this state. When turning on an electric field, those holes can be excited to the continuum by impact ionization and then accelerate toward the energy of the resonant state. Once they reach that energy, scattering is intense and the holes may again be captured by the acceptors but in a relatively high level. Note that the time scales for the impact ionization and scattering is small and of order of picosecond. Consequently the radiative decay from higher to lower acceptor levels of microsecond time scale is relatively slow and a population inversion can be achieved as long as the lower localized levels are depopulated by impact ionization.
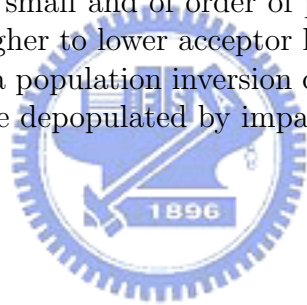
Chapter 2

Resonant state laser in quantum well structure

2.1 The limit on photon energy in RSL

In the previous approach to RSL[10, 11, 12, 13] there is a serious constraint on the emitted photon energy. In single QW the acceptor level splitting needs to be greater than the impurity binding energy in order to have resonant state. The photon energy therefore must be larger than the binding energy, which is several tens of meV (15 meV for Ge and 50 meV for Si[14]) corresponding to more than 10 THz. In this paper we present a concept of Silicon-Germanium QW RSL which is free of such a constraint. Instead of one single QW, in our structure the continuous and localized states are in different layers and the resonance can be controlled by independent strains in different layers. Therefore resonant scattering can occur even if the energy splitting is smaller than the acceptor binding energy. Silicon-Germanium alloy is chosen as the material system for this concept because of its low absorption in the THz range and easy integration with Si electronics. We calculate the energies of the localized acceptor levels and continuous sub-band levels (indicated as "continuum" below), and give the relation between the emitted photon energy and the structure parameters. In order to show that population inversion can be realized under practical experimental conditions, we construct a comprehensive theoretical model for non-equilibrium behaviors of holes in the QW structure and study in detail the the dynamical behaviors of the holes with external pumping field. Our results indicate that emission as low as 1 THz can be obtained in the QW structure with reasonable Germanium compositions under an electric field of about 100 V/cm at 10 K.
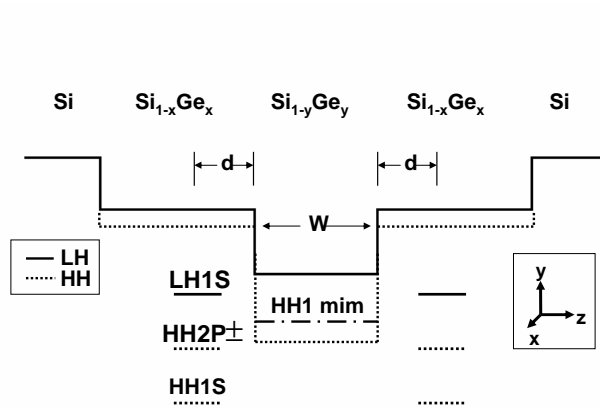
Figure 2.1: The band edge profiles for light hole (LH, solid line) and heavy hole (HH, dashed line) of the proposed QW structure are shown. Both **x** and **y** directions are perpendicular to the crystal growth direction **z**. x and y are the Germanium compositions for the well and barrier layers respectively. W is the well width. The energies of the strain-split acceptor levels LH1S, HH1S and HH2P± relevant for THz laser are also shown. d is the distance between the dopant and the boundary of the well. The HH1 minimum is indicated by the dash-dot line. The insert defines the directions in the system.

2.2   A remedy: QW-RSL

The profile of valence band edge diagram along crystal growth direction (**z** direction) of the proposed QW structure is shown in Fig. 2.1. For clarity the sign of energy is reversed. The splitting of heavy hole and light hole band edge is due to strain caused by lattice mismatch between SiGe alloy and Si. The strain can be linearly related to the Germanium compositions in the alloy. The two $Si_{1-x}Ge_x$ layers sandwiching the central $Si_{1-y}Ge_y$ layer have identical profile and are δ-doped with identical acceptor density n_a. The profile has been designed to be symmetric for simpler theoretical treatments.

As can be seen in the profile of the heavy hole band edge in Fig. 2.1, holes are confined in the central layer in the **z** direction due to the potential barriers constituted by the two identical $Si_{1-x}Ge_x$ layers at two sides. Series of subbands are formed due to the confinement. We label the energy minimum of the first heavy hole subband (HH1), which is a function of the well width W, by the dash-dot line in the central layer. In addition there is a series of localized acceptor levels attached to the heavy hole band edge in each δ-doped layer. We focus on the low-lying heavy hole $2p_{\pm 1}$ level (HH2P±), labeled by a short dashed line, and the light hole acceptor $1s$ level (LH1S) labeled by a short solid line. LH1S and HH2P± have opposite parity and

12
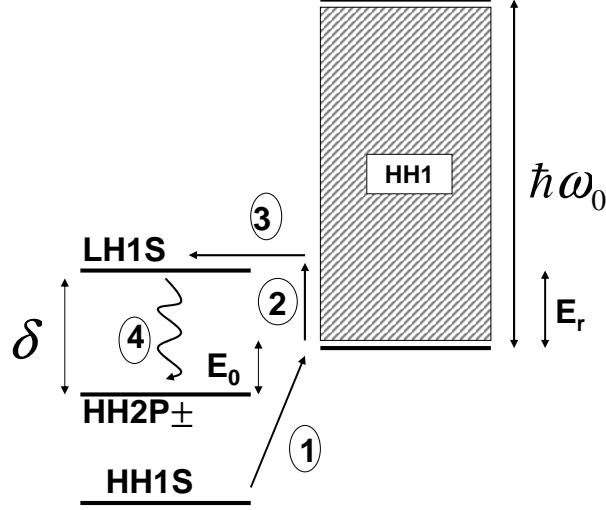
Figure 2.2: Schematic 4-level operation of the THz laser. The operation involves three acceptor states LH1S, HH1S and HH2P$\pm$ as well as the HH1 continuum (shaded region). The four major processes are also indicated. Process 1 indicates the field ionization of HH1S through the a barrier to reach HH1 minimum. The low-energy holes in HH1 are pumped toward resonant states by electric field in the Process 2. Process 3 represents resonant capture of continuum holes of energy E_r to meta-stable LH1S. The radiative decay by stimulated emission into the lower localized state HH2P$\pm$ is denoted by Process 4.

hence are expected to give the strongest intensity of radiation among all possible transitions. Besides, the acceptor 1s level attached to the heavy hole band edge is the very lowest state for holes in the system and is labeled by HH1S, which is shown below the HH2P$\pm$ in Fig. 2.1. With precise control of Germanium compositions x and y in the QW structure, the heavy hole and light hole band edges as well as the localized acceptor levels can be adjusted to have the relative energies required for THz laser.

2.3 Mechanism for population inversion

Now we consider the pumping mechanism of the holes under an external electric field $\mathbf{F}$ (strength F) perpendicular to the $\mathbf{z}$ direction, say $\mathbf{x}$ direction. The physical picture is shown in Fig. 2.2. HH2P$\pm$ is below LH1S and

minimum of HH1 by δ and E_0 respectively. Note that in our problem δ must be larger than E_0 to have resonance between HH1 and LH1S. At zero temperature all the holes stay in the low-lying HH1S state without field. When the external electric field is applied, some holes on HH1S are initially field-ionized then more holes are excited to HH1 through impact ionization and acquire more kinetic energy until occurrence of phonon scattering. The processes of field ionization and pumping of holes are denoted by Process 1 and 2 respectively in Fig. 2.2. Another channel for slowing down the holes in HH1 is the resonance capture by LH1S. The transition between heavy hole and light hole states, denoted by Process 3, is facilitated by the off-diagonal matrix element[11] of Luttinger-Kohn Hamiltonian to be discussed below. As the occupation of higher LH1S grows with increasing external field and the lower HH1S and HH2P$\pm$ are gradually depleted by impact ionization, a population inversion is expected. Emission of THz photon, indicated by Process 4, will take place due to the radiative decay of holes from LH1S to HH2P$\pm$.

The resonance of the localized state and the continuum is achieved by raising the strain of the lattice so that the localized state is lifted to immerse within the continuum. In the previous works on QW RSL[12, 13] this acceptor impurity is doped in the same layer as the continuous states, so E_0 is simply the binding energy. Apparently in such case the strain splitting δ must exceed the binding energy, corresponding to a lower bound of photon energy. In this work we spatially separate the acceptor impurity and quantum well so the relative energy between the localized state and continuum has a much higher flexibility by adjusting the compositions x, y and the well width W. As a result no matter how small δ is we can always adjust the QW structure such that $E_0 < \delta$. However the only lower bound for the emitted photon energy is the energy shift of the resonant state caused by the perturbation of the continuum as discussed previous Section. Hence our proposed structure is able to emit photon of energy less than the binding energy which is usually several tens of meV (12 THz in the case of Si) and is expected to fulfill the needs of solid-state optical sources of several THz or even sub-THz range. Because the relative energies of the localized and continuous states are crucial to the laser operation, below we calculate the quantitative relations between the relevant levels in the QW structure and QW parameters like width W and Germanium compositions. Even though the acceptor levels are outside the central well, there is no difficulty for the holes in the central well to be resonantly captured by the acceptor as long as there is a overlap between the wavefunctions of the acceptor levels and HH1. In order for the above picture to be valid, it is important to choose an intermediate value for the distance between the dopants and the quantum

well. The distance should be neither so large relative to the acceptor Bohr radius that there is no overlap between the acceptor level and quantum well level nor so small that acceptor level itself becomes heavily influenced by the well.

Chapter 3

Theoretical modeling of population inversion in a continuum-trap system

3.1 Hybridization of acceptor impurity state and valence band continuum

3.1.1 Subband and Impurity Wavefunctions

In this subsection we calculate the wavefunctions and energies of the relevant states. We first consider a perfect crystal. The wavefunctions for the heavy hole and light hole bands can be represented by the eigenfunctions of the Luttinger-Kohn Hamiltonian[15] H_{LK} in the Bloch function basis $\{u_{3/2}, u_{1/2}, u_{-1/2}, u_{-3/2}\}$, which is the periodic sum of the atomic orbitals with total angular momentum quantum number $j = \frac{3}{2}$. The subscripts stand for their **z** component j_z of total angular momentum j. The column vector Ψ formed by the envelope functions $\{\varphi_{3/2}(r), \varphi_{1/2}(r), \varphi_{-1/2}(r), \varphi_{-3/2}(r)\}$ are the eigenfunctions of H_{LK}. The true wavefunction $\psi(r)$ of the state is given by $\psi(r) = \Sigma_\tau \varphi_\tau(r) u_\tau$. The Luttinger-Kohn Hamiltonian can be written as

$$H_{LK} = \frac{\hbar^2}{2m_0} \begin{pmatrix} \hat{a}_+ & \hat{b} & \hat{c} & 0 \\ \hat{b}^\dagger & \hat{a}_- & 0 & \hat{c} \\ \hat{c}^\dagger & 0 & \hat{a}_- & -\hat{b} \\ 0 & \hat{c}^\dagger & -\hat{b}^\dagger & \hat{a}_+ \end{pmatrix} \begin{matrix} j_z = \frac{3}{2} \\ j_z = \frac{1}{2} \\ j_z = -\frac{1}{2} \\ j_z = -\frac{3}{2} \end{matrix} \, , \tag{3.1}$$

and the matrix elements are

$$\hat{a}_+ = -\hat{k}_z(\gamma_1 - 2\gamma)\hat{k}_z - (\gamma_1 + \gamma)(\hat{k}_x^2 + \hat{k}_y^2) \, , \tag{3.2}$$
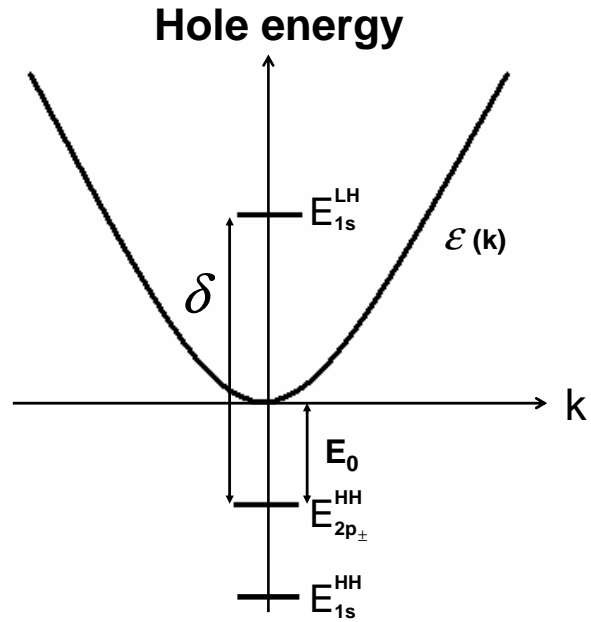
16

Figure 3.1: Spectrum of the diagonal part H^0 of the full Hamiltonian H. The acceptor states of interest and the continuous HH1 are shown. The binding energy for HH2P± and the emitted photon energy are denoted by E_0 and δ respectively. Their values and corresponding variational Bohr radius is shown in Table I. $\varepsilon(\mathbf{k})$ is the spectrum of subband HH1.

$$\hat{a}_- = -\hat{k}_z(\gamma_1 + 2\gamma)\hat{k}_z - (\gamma_1 - \gamma)(\hat{k}_x^2 + \hat{k}_y^2) \,, \tag{3.3}$$

$$\hat{b} = \sqrt{3}(\hat{k}_x - i\hat{k}_y)(\gamma\hat{k}_z + \hat{k}_z\gamma) \,, \tag{3.4}$$

$$\hat{c} = \sqrt{3}\gamma(\hat{k}_x - i\hat{k}_y)^2 \,. \tag{3.5}$$

m_0 is the free electron mass and $\hat{k}_i = i\frac{\partial}{\partial x_i}$, $i = x, y, z$ are operators for the envelope functions. γ_1, γ_2 and γ_3 are material-dependent Luttinger parameters and $\gamma = (2\gamma_2 + 3\gamma_3)/5$. For crystals with translational invariance the envelope functions are all proportional to plane waves $e^{i\mathbf{k}\cdot\mathbf{r}}$ and the above operators turn into c-numbers. Diagonalization of the matrix gives the spectrum $E_\pm(\mathbf{k})$ which possesses four-fold degeneracy at the band edge. The sign $\pm$ indicates that there are two branches, the heavy hole and light hole bands. The spectrum $E_\pm(\mathbf{k})$ is given by

$$E_\pm(\mathbf{k}) = \frac{\hbar^2}{m_0}\left[\gamma_1\frac{k^2}{2} \pm \sqrt{\gamma_2^2 k^4 + 3(\gamma_3^2 - \gamma_2^2)(k_x^2 k_y^2 + k_y^2 k_z^2 + k_z^2 k_x^2)}\right] \,. \tag{3.6}$$

When the perfect crystal is subject to a stress due to external strain or lattice mismatch the crystal symmetry is lowered, and the four-fold degeneracy at the valence band edge is split into two two-fold degeneracies. If the strain is along the [001] axis, which is parallel to the $\mathbf{z}$ direction, this effect is to add a strain term V_{st} to the Hamiltonian.[16] It can be represented by the diagonal matrix

$$V_{st} = \begin{pmatrix} \zeta & 0 & 0 & 0 \\ 0 & -\zeta & 0 & 0 \\ 0 & 0 & -\zeta & 0 \\ 0 & 0 & 0 & \zeta \end{pmatrix} \,. \tag{3.7}$$

The coincidence of heavy hole band and light hole band at band edge is split by the strain factor ζ which is proportional to external force and dependent on the direction of strain. In QW the strain results from the lattice mismatch between Si and SiGe alloy. In epitaxially grown SiGe QW structure on Si substrate, the lattice constant of the whole structure is fixed by the Si lattice constant. Because the natural lattice constant of SiGe alloy is different from Si, there must be a strain in the alloy to force the lattice constant to match Si. The relation between valence band splitting ζ due to strain and the Germanium composition t in $Si_{1-t}Ge_t$ alloy was studied before.[17] The expression in eV is $\zeta(t) = 0.01 + 0.2t - \frac{1}{4}\sqrt{0.0016 + 0.0074t + 0.24t^2}$. In our proposed QW structure the Germanium compositions vary in the $\mathbf{z}$ direction and the hence the strain factor ζ is a function of z.

For an acceptor in the stressed crystal we shall add the Coulomb potential V_I due to the charged center

$$V_I(r) = v_I(r)I = \frac{1}{4\pi\epsilon}\frac{e}{r}I \, , \tag{3.8}$$

where ϵ is the dielectric constant. r is the distance from the acceptor. I represents the 4×4 identity matrix. In the high strain limit the off-diagonal coupling $\hat{b}$ and $\hat{c}$ can be considered as perturbations and H_{LK} becomes approximately diagonal with two-fold degeneracy for heavy and light holes. The resultant localized states can also be divided into two subgroups like the band states.

After reviewing the bulk crystals we can extend the discussions to the states in QW structures shown in Fig. 2.1. Even without strain the valence band edge depends on the Germanium compositions,[18] described by $V_b(z) = v_b(z)I$. For $Si_{1-t}Ge_t$ alloy grown on Si, the valence band offset in eV can be written as $v_b = 0.84t$. The total band edge profile in Fig. 2.1 comes from the sum of $V_b(z)$ and $V_{st}(z)$. The Luttinger parameters have different values in different layers, hence they are functions of z. Homogeneity of those parameters is assumed within each Silicon-Germanium layer and their values are determined by linear interpolation between pure Si and pure Ge. The heavy hole and light hole subbands in the structure can be expressed by the total Hamiltonian H

$$H = H_{LK} + V_b(z) + V_{st}(z) \, . \tag{3.9}$$

Note that $z=0$ is at the center of well so there is a parity symmetry with respect to $z \to -z$ in this problem. Here we separate H_{LK} into diagonal and off-diagonal parts, labeled by H_{LK}^0 and H_{LK}^1 respectively. The wavefunctions for HH1 emerge from eigenfunctions of diagonal parts $H^0 = H_{LK}^0 + V_b(z) + V_{st}(z)$ of the full Hamiltonian H. The off-diagonal heavy hole-light hole mixing H_{LK}^1 will be considered later as a perturbation. The unperturbed Schrödinger equation can be written as

$$H^0\Psi = \epsilon\Psi \, . \tag{3.10}$$

We solve this to obtain HH1 envelope functions Ψ of the wavefunctions $\psi_{\mathbf{k}}$ with eigenvalues $\varepsilon(\mathbf{k})$. On the other hand, the localized states ϕ_{1s}^{LH} and $\phi_{2p_\pm}^{HH}$ with respective eigenvalues E_{1s}^{LH} and $E_{2p_\pm}^{HH}$ are eigenstates of Hamiltonian $H_{LK}^0 + V_I(r) + [V_b(z) + V_{st}(z)]_{z=z_0^\pm}$. $z_0^\pm \equiv \pm(\frac{W}{2} + d)$ denote the positions of acceptors. The implicit assumption is that the Coulomb potentials V_I has little effect on the subband wavefunctions while the non-uniform strain is irrelevant to the localized state. The above approximations are justified

by the conditions that the distance between the dopant and quantum well boundary d as well as the thickness of outer $Si_{1-x}Ge_x$ layers are both larger than the acceptor Bohr radius. The equations turn out to be the typical one-dimensional potential well problem for the subband and hydrogen atom problem for the localized states. Energy spectrum for the relevant states are shown in Fig. 3.1. The explicit wavefunctions for HH1 can be expressed as

$$\psi_{\mathbf{k}}(\rho, z) = \frac{1}{\sqrt{A}} g(z) e^{i\mathbf{k}\cdot\vec{\rho}} u_{\pm 3/2} , \tag{3.11}$$

where the $\pm$ sign in the wavefunctions reflects the two-fold degeneracy guaranteed by time-reversal symmetry in the absence of magnetic field and the envelope function $g(z)$ have the even parity to yield the lowest energy of all subbands. A is the QW area. $\vec{\rho} = (x, y)$ is the in-plane coordinate. The acceptors wavefunction localized at $z = z_0^{\pm}$ and $\vec{\rho} = 0$ are of the forms

$$\phi_{1s}^{LH}(\vec{\rho}, z) = \varphi_{1s}\left[\vec{\rho}, z - z_0^{\pm}\right] u_{\pm 1/2} , \tag{3.12}$$

$$\phi_{2p_\pm}^{HH}(\vec{\rho}, z) = \varphi_{2p_\pm}\left[\vec{\rho}, z - z_0^{\pm}\right] u_{\pm 3/2} , \tag{3.13}$$

where $\pm$ stands for $z > 0$ and $z < 0$ respectively. We use hydrogenic trial functions

$$\varphi_{1s}(\vec{\rho}, z) = \frac{1}{\sqrt{\pi a^2 b}} \exp\left(-\sqrt{\frac{\rho^2}{a^2} + \frac{z^2}{b^2}}\right) , \tag{3.14}$$

$$\varphi_{2p_\pm}(\vec{\rho}, z) = \frac{1}{2\pi a^4 b} \rho e^{i\phi} \exp\left(-\sqrt{\frac{\rho^2}{a^2} + \frac{z^2}{b^2}}\right) . \tag{3.15}$$

a (in-plane Bohr radius) and b (out-of plane Bohr radius) are variation parameters for minimizing their energy and ϕ is the polar angle in the **xy** plane. ρ is the modulus $|\vec{\rho}|$. Variational calculations are performed to obtain the acceptor level splitting δ and the difference E_0 between HH2P$\pm$ and HH1 minimum. Variational calculations are performed to obtain the acceptor level binding energy. The resultant binding energies and the variational Bohr radius of the levels of interest are shown in Table I.

Next we consider the corrections to the impurity states resulting from the QW confinement potential as well as the off-diagonal couplings with the HH1 continuum. Such corrections are necessary for having a more precise prediction on the emitted photon energy. Here we focus on the corrections to the binding energy of LH1S, which is resonant with the continuum. Note that the binding energy is relative to the barrier, not the quantum well continuum.

The expressions for the corrections ΔE_{1s} are given below and the details of derivation are presented in Appendix 4.1.

$$\Delta E_{1s} = \Delta + P\frac{A}{(2\pi)^2}\int d\mathbf{k}\frac{|\alpha_{\mathbf{k}}|^2}{E_{1s} - \varepsilon_{\mathbf{k}}} \ . \tag{3.16}$$

Δ is the correction due to the confinement potential while the integral due to the coupling with the continuum. P stands for the Cauchy principle value integration. $\alpha_{\mathbf{k}}$ and Δ are given by

$$\alpha_{\mathbf{k}} = \langle\varphi_{1s}|\hat{c}|\psi_{\mathbf{k}}\rangle \ , \tag{3.17}$$
$$\Delta = \langle\varphi_{1s}|\left[v_C(z) - v_C(z_0)\right]|\varphi_{1s}\rangle \ . \tag{3.18}$$

Note that only the off-diagonal elements involving k_x and k_y are considered because the resonance requires a large in-plane momentum. The confinement potential v_C is the diagonal element of $V_b + V_{st}$ belonging to light hole states. Correction due to the confinement potential Δ is negligible in the present case because very little portion of the impurity wavefunction for the impurity falls on the QW region and the confinement potential is small compared to the impurity binding energy. In fact our calculation shows this correction on E_{1s} is less than 0.1 %. However this effect for the case of smaller binding energy is important such as the shallow donors located in the barrier near the quantum well.[19] The second term resembles the formula for second order perturbation. Even though still only about 10 % of E_{1s}, it provides significant corrections in case of the small emitted photon energy. The smallness of the corrections is reasonable since the light hole localized states and the heavy hole continuum have small overlap and they can couple to each other only though the off-diagonal elements of H_{LK} which is treated as perturbation in the high-strain limit.[11] The QW continuum and the HH2P$\pm$ are assumed to be unaffected by the perturbation.

3.1.2 Resonant transition

The hybridization of the localized LH1S and the HH1 continuum via the off-diagonal perturbation H_{LK}^1 leads to a new set of resonant states $\{\Psi_E\}$ labeled by its complex energy $E + i\frac{\Gamma_E}{2}$. The imaginary part is given by

$$\frac{\Gamma_E}{2} = \pi\frac{A}{(2\pi)^2}\int d\mathbf{k}\delta(E - \varepsilon_{\mathbf{k}})|\alpha_{\mathbf{k}}|^2 \ . \tag{3.19}$$

The nonzero imaginary energy Γ_E here represents that Ψ_E is a quasi-stationary state. More precisely speaking the HH1 holes of momentum $\mathbf{k}$ can be captured by LH1S with the transition rate $W_{\mathbf{k}}^{res}$ for a time interval $\hbar/\Gamma$. The
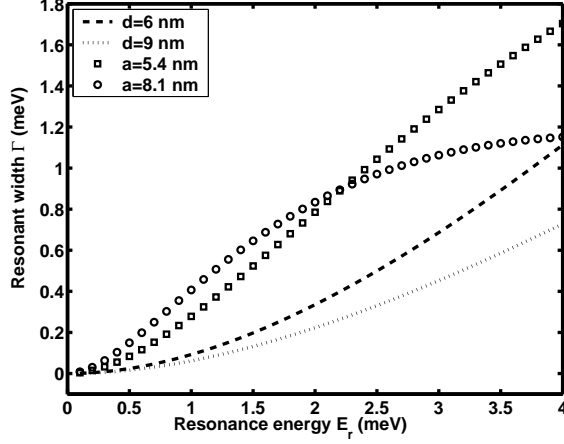
Figure 3.2: The energy width Γ of the resonant state is shown as a function of the resonant state energy E_r measured from HH1 minimum. Symbol curves correspond to various in-plane Bohr radius a of LH1S orbital with fixed $d = 6$ nm. Dash and dot lines correspond to various distance d between the acceptor and boundary of the central well with $a = 2.7$ nm.

transition rate and the time interval are determined in a self-consistent manner, that is

$$W_{\mathbf{k}}^{res} = \frac{2}{\hbar}|\alpha_{\mathbf{k}}|^2 \frac{\Gamma/2}{[\varepsilon(\mathbf{k}) - E_{1s}]^2 + \Gamma^2/4} , \tag{3.20}$$

$$\frac{\Gamma}{\hbar} = \sum_{\mathbf{k}} W_{\mathbf{k}}^{res} . \tag{3.21}$$

The center of the Lorentzian corresponds to E_{1s} because the resonant state $\Psi_{E_{1s}}$ contains the maximum component of the localized LH1S. For simplicity we regard the unknown Γ in Eq. (3.20) as close to zero and the Lorentzian is reduced to a delta function. So long as the resultant Γ from Eq. (3.21) is small compared to the resonance energy $E_r \equiv E_{1s} - \varepsilon(\mathbf{k} = 0)$ (see Fig. 2.2, 3.1) of LH1S, this method is self-consistent to obtain Γ.

Next work out Γ in the small Γ limit. In other words the resonant transition rate $W_{\mathbf{k}}^{res}$ can be given simply by the Fermi-Golden rule,

$$W_{\mathbf{k}}^{res} = \frac{2\pi}{\hbar}|\alpha_{\mathbf{k}}|^2 \delta\left[\varepsilon(\mathbf{k}) - E_{1s}\right] . \tag{3.22}$$

In order to obtain an explicit expression for the transition rate we need to

22

calculate the overlap integral $\langle \varphi_{1s} | \psi_{\mathbf{k}} \rangle$. Assuming the main contribution to this integral comes from the region in the barrier, i.e. $|z| > \frac{W}{2}$, we arrive at

$$
\begin{aligned}
\langle \varphi_{1s} | \psi_{\mathbf{k}} \rangle &= \frac{1}{\sqrt{A}} \frac{1}{\sqrt{\pi a^2 b}} \int dz\, g(z) \int dxdy\, e^{i\vec{k}\cdot\vec{\rho}} \exp\left(-\sqrt{\frac{\rho^2}{a^2} + \frac{z^2}{b^2}}\right) \\
&= \aleph \sqrt{\frac{16\pi a b^2}{A}} \frac{1}{\eta^2} \left\{ e^{-\eta\frac{d}{b}} \frac{1}{\kappa b - \eta}\left[\frac{\kappa b - 2\eta}{\eta(\kappa b - \eta)} + \frac{d}{b}\right] + e^{-\kappa d}\left[\frac{(2\eta - \kappa b)}{\eta(\kappa b - \eta)^2} + \frac{(2\eta + \kappa b)}{\eta(\kappa b + \eta)^2}\right]\right\}.
\end{aligned}
\tag{3.23}
$$

The dimensionless quantity $\eta \equiv \sqrt{1 + a^2 k^2}$ is introduced. $\aleph$ is to normalize the envelope function $g(z)$ as $\int \aleph^2 |g(z)|^2 dz = 1$. κ is the decay constant of $g(z)$ in the barriers.

Γ as a function of resonance energy E_r is plotted in Fig. 3.2 for various acceptor in-plane Bohr radius a and separation d. The effect of coupling with the continuum can be investigated through Γ. For distance d much larger than the Bohr radius, the coupling is diminished due to decreasing overlap between the impurity state and the continuum. In such case the formation of resonant state is impossible. However the dependence of the coupling on the Bohr radius is determined by two competing factors. Namely in the **z** direction the envelope function $g(z)$ of continuum has larger overlap with localized impurity state of larger Bohr radius, while in the **xy** plane the continuum of higher kinetic energy can only be coupled to the impurity state of smaller Bohr radius because such localized state has larger Fourier momentum components. For larger Bohr radius, it is shown in Fig. 3.2 that Γ is larger at lower E_r while it is smaller at higher E_r.

3.2 Carrier kinematics in the steady electric field

So far there is no comprehensive theoretical model for the non-equilibrium behavior of acceptor levels interacting with a subband in QW. In order to make quantitative predictions of the conditions for hole population inversion, below we construct a model which takes into account of all the relevant physical processes for such system.

3.2.1 Hole Statistics at equilibrium

The occupation probabilities of LH1S, HH2P$\pm$, HH1S and HH1 states are indicated by f_1, f_2, f_g and $f_{\mathbf{k}}$ respectively. In thermal equilibrium the occupation ratio of LH1S to HH2P$\pm$ is given by the Boltzmann factor, i.e.

$f_2/f_1 = \exp(-\beta\delta)$. β is the inverse of the product of Boltzmann constant k_B and temperature T. Moreover at equilibrium the hole densities are determined by assigning each level with its Boltzmann weighting. Note the all the holes are provided by the lowest localized level and hence we have the following normalization of total holes.

$$n_a f_g + n_a f_1 + \frac{1}{A} \sum_{\mathbf{k}} f_{\mathbf{k}} + n_a f_2 = n_a \,. \tag{3.24}$$

When the electric field is turned on holes acquire kinetic energy from the external field and the distribution of holes deviates from Boltzmann distribution. In order to give a quantitative account of how the non-equilibrium populations depend on parameters (e.g. field strength F, temperature T, and acceptor density n_a), we need to study the microscopic kinetics governing the transitions among the states.

3.2.2 Boltzmann Kinematic Equation

The strategy for obtaining the non-equilibrium populations is as follows. First we neglect the low-lying HH2P± and HH1S temporarily and solve the kinetics of the subsystem containing HH1 and LH1S in order to obtain the relation between f_2 and $f_{\mathbf{k}}$, with considerations of phonon scattering within HH1 and the resonant transition between the continuous HH1 and the localized LH1S. This is justified because the resonant scattering is much faster than the decay through spontaneous emission from LH1S to HH2P±.[10] Afterwards the occupation probability f_1 of HH2P± is determined by the its balance with non-equilibrium subband distribution $f_{\mathbf{k}}$ through impact ionization, thermal recombination, and their inverse processes Auger recombination and thermal excitation. Detailed calculations are given below.

For a given number of holes in the subsystem containing HH1 and LH1S, the non-equilibrium distribution $f_{\mathbf{k}}$ in HH1 and occupation of LH1S f_2 are studied by solving the Boltzmann kinetic equation numerically for various electric fields and acceptor densities. In the subsystem the holes in HH1 acquire kinetic energy from the constant electric field $\mathbf{F}$ applied along the $\mathbf{x}$ axis. For moderate electric field and low temperature, it is adequate to adopt the concept of *streaming motion*[22] in which the only significant scattering is due to optical phonon (energy $\hbar\omega_0$). This is implemented by introducing a particle drain in momentum space such that once a specific hole drifts with velocity $e\mathbf{F}/\hbar$ through the energy surface $\varepsilon = \hbar\omega_0$ (denoted by Π) in the momentum space, the hole will experience a optical phonon scattering and simultaneously reemerge as a hole of energy less than ϵ_0.[10, 11] Hence $f_{\mathbf{k}} = 0$ for $\varepsilon(\mathbf{k}) \geq \hbar\omega_0$. The energy ϵ_0 is determined by the requirement

24

that in the presence of constant electric field $\mathbf{F}$ the probability for a hole being able to drift beyond the constant energy surface $\varepsilon = \hbar\omega_0 + \epsilon_0$ without emitting one optical phonon is negligibly small. The quantity ϵ_0 is equal to the product of external force eF, carrier velocity $\sqrt{2m^*\hbar\omega_0}/\hbar$ and inverse of the average optical phonon emitting rate ν_A. m^* stands for the effective mass. Note that the energy-independent optical phonon emitting rate is due to the constant density of states in two dimension. Therefore the excess energy can be expressed as

$$\epsilon_0 = \frac{eF}{\nu_A}\sqrt{\frac{2\hbar\omega_0}{m^*}} \ . \tag{3.25}$$

The reemerging holes can be modeled as a particle source[10, 11]

$$S(\mathbf{k}, t) = \frac{\frac{e}{\hbar}\left[\int_\Pi f_\mathbf{k}(t)\mathbf{F} \cdot d\mathbf{S}\right]}{\left[\int \Theta(\epsilon_0 - \varepsilon(\mathbf{k}'))d^2k'\right]}\Theta(\epsilon_0 - \varepsilon(\mathbf{k})) \ , \tag{3.26}$$

where Θ is the step function. The meaning of the above expression is that the holes reemerging rate is uniform for energy within ϵ_0, and the total reemergence rate must match the collection of the outward carrier flux $\frac{e\mathbf{F}}{\hbar}f_\mathbf{k}$ passing through the surface Π in the momentum space.

In order to properly account for the temperature effects, we include the acoustic phonon scattering. The acoustic phonon scattering rate $W_{\mathbf{k},\mathbf{k}'}^{acu}$ is of the form[23]

$$W_{\mathbf{k},\mathbf{k}'}^{acu} = \frac{2\pi\Xi^2 q^2}{\varrho\omega_\mathbf{q}WA}(n_q + \frac{1}{2} \mp \frac{1}{2})\delta\left[\varepsilon(\mathbf{k}') - \varepsilon(\mathbf{k}) \mp \hbar\omega_\mathbf{q}\right] \ , \tag{3.27}$$

where ϱ is the mass density of solid lattice and Ξ is the lattice deformation potential. The acoustic phonon involved in the transition has wave number $\mathbf{q} = \mathbf{k}' - \mathbf{k}$ and its dispersion is given by $\omega_\mathbf{q} = cq$ where c is the sound velocity in the solid. Emission and absorption of phonon in the processes correspond to $+$ and $-$ respectively. The product WA represents the QW volume.

We assume homogeneity in the $\mathbf{x}$ and $\mathbf{y}$ directions so that the distribution are function of variables k_x and k_y only. The set of kinetic equations can be written as

$$\frac{\partial f_\mathbf{k}}{\partial t} + \frac{e\mathbf{F}}{\hbar} \cdot \frac{\partial f_\mathbf{k}}{\partial \mathbf{k}} = S_\mathbf{k} - D_\mathbf{k} + C_1\left[f_\mathbf{k}, f_2\right] \ , \tag{3.28}$$

$$\frac{\partial f_2}{\partial t} = C_2\left[f_\mathbf{k}, f_2\right] \ . \tag{3.29}$$

$C_i\left[f_\mathbf{k}, f_2\right], i = 1, 2$ represent the collision terms for the acoustic phonon and resonant scattering. They are functionals of the the distribution functions. The explicit expression for the collision terms are

$$C_1[f_\mathbf{k}, f_2] = n_a A \left\{ W_\mathbf{k}^{res} (f_2 - f_\mathbf{k}) \right\} + \sum_{\mathbf{k}'} \left\{ W_{\mathbf{k}'\mathbf{k}}^{acu} f_{\mathbf{k}'} - W_{\mathbf{k}\mathbf{k}'}^{acu} f_\mathbf{k} \right\} , \quad (3.30)$$

$$C_2[f_\mathbf{k}, f_2] = \sum_\mathbf{k} W_\mathbf{k}^{res} (f_\mathbf{k} - f_2) . \quad (3.31)$$

The kinetic equations Eq. (3.28) and Eq. (3.29) are solved numerically by starting with the equilibrium distribution and then integrating forward in time until a steady state is reached. Note that the sum of densities $n_a f_2 + \frac{1}{A} \sum_\mathbf{k} f_\mathbf{k}$ is a conserved quantity in the time evolution, guaranteed by cancelation of collision terms and the boundary conditions at surface Π. In this way not only the steady state but also the transient of the system can be modeled. The occupations of LH1S f_2 and the HH1 $f_\mathbf{k}$ are obtained up to an arbitrary total number of holes in the subsystem. In particular the relation between f_2 and $f_\mathbf{k}$ at steady state can be readily seen by setting the left hand side of Eq. (3.29) equal to zero

$$f_2 = \frac{\sum_\mathbf{k} W_\mathbf{k}^{res} f_\mathbf{k}}{\sum_\mathbf{k} W_\mathbf{k}^{res}} = \int d\varepsilon \delta \left[\varepsilon(\mathbf{k}) - E_r \right] f_\mathbf{k} . \quad (3.32)$$

Now we consider the special case with no electric field. The subsystem is in thermal equilibrium. The occupations of HH1 and LH1S obey the Boltzmann statistics guaranteed by the presence of delta function in the expression for resonant scattering as well as the fact that the scattering between HH1 states $\mathbf{k}$ and $\mathbf{k}'$ due to acoustic phonon emission and absorption satisfies the relations

$$\frac{W_{\mathbf{k}'\mathbf{k}}^{acu}}{W_{\mathbf{k}\mathbf{k}'}^{acu}} = \frac{1 + n_\mathbf{q}}{n_\mathbf{q}} = \exp \left\{ -\beta \left[\varepsilon(\mathbf{k}') - \varepsilon(\mathbf{k}) \right] \right\} . \quad (3.33)$$

$\varepsilon(\mathbf{k}') > \varepsilon(\mathbf{k})$ is assumed without loss of generality and $\mathbf{q}$ is the wavevector of the phonon involved in the process. Therefore in equilibrium f_2 is given by

$$f_2 = \frac{N/A}{\frac{1}{A} \sum_\mathbf{k} e^{-\beta \varepsilon(\mathbf{k})} + n_a e^{-\beta E_r}} e^{-\beta E_r} , \quad (3.34)$$

where N represents the total number of holes in the subsystem.

In order to describe the effect of the electric field on the distribution, we define a dimensionless parameter $\lambda(F, T)$ by

$$\lambda(F, T) \equiv \frac{\frac{1}{A} \sum_\mathbf{k} f_\mathbf{k}}{n_a f_2 + \frac{1}{A} \sum_\mathbf{k} f_\mathbf{k}} = \frac{n_s}{n_2 + n_s} . \quad (3.35)$$
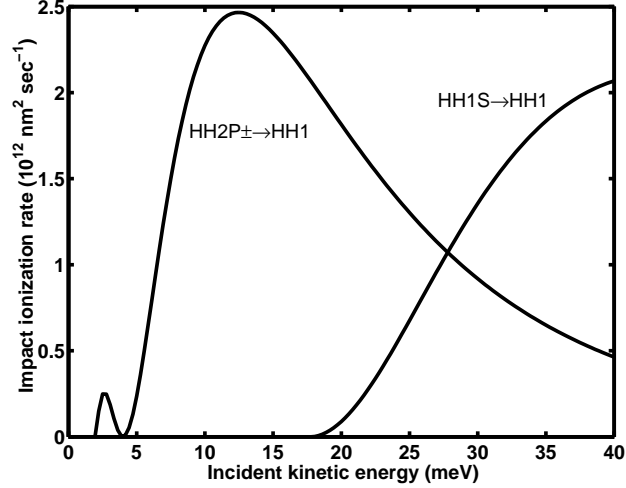
26

Figure 3.3: Impact ionization rates w^{ip} as functions of kinetic energy ε of incident subband hole for HH1S to HH1 and HH2P$\pm$ to HH1 are respectively shown.

$\lambda(F, T)$ is the fraction of holes in HH1 for the subsystem. For low temperature at equilibrium virtually all holes stay near the HH1 minimum so λ is close to unity. In the presence of the electric field the population of LH1S increases as a consequence of Eq. (3.32), since holes in HH1 acquire kinetic energy from field so the non-equilibrium distribution $f_{\mathbf{k}}$ has larger value at $\varepsilon(\mathbf{k}) = E_r$. Therefore for given n_a, $\lambda(F, T)$ is expected to decrease as electric field increases. Increase of acceptor density n_a also raise f_2 because the distribution in HH1 becomes more concentrated on $\varepsilon(\mathbf{k}) \leq E_r$. This is because the stronger resonance scattering inhibits the holes to acquire energy higher than the resonance energy E_r.

3.2.3 Impact Ionization and thermal recombination rates

Next we turn to the interactions between HH1 and low-lying localized states including HH1S and HH2P$\pm$. The interactions are dominated by impact ionization and the thermal recombination as well as their inverse processes. In impact ionization process one energetic hole in HH1 with momentum $\mathbf{k}$ scatters with one hole in the low-lying localized states ϕ_b in the barrier through the Coulomb interaction such that they both come out as free holes in HH1. The transition rate is given by

$$w^{ip}(\mathbf{k}) = \frac{2\pi}{\hbar} \sum_{\mathbf{k_1},\mathbf{k_2}} \left| \left\langle \mathbf{k_1}, \mathbf{k_2} \left| \frac{e^2}{r} \right| \mathbf{k}, b \right\rangle \right|^2 \delta \left[\varepsilon(\mathbf{k}) - E_b - \varepsilon(\mathbf{k_1}) - \varepsilon(\mathbf{k_2}) \right], \quad (3.36)$$

where r is the separation between the incident hole and localized hole. The summation is over all the final two particle Bloch states $(\mathbf{k_1}, \mathbf{k_2})$. The first task is to evaluate the scattering matrix element $\langle \mathbf{k_1}, \mathbf{k_2} | \frac{e^2}{r} | \mathbf{k}, b \rangle$. Substituting the explicit expressions for those localized wavefunctions and Coulomb potential into the scattering matrix element, it becomes

$$\int d^3\mathbf{r_1} d^3\mathbf{r_2} \frac{1}{\sqrt{A}} e^{-i\mathbf{k_1}\cdot\vec{\rho}_1} f^*(z_1) \frac{1}{\sqrt{A}} e^{-i\mathbf{k_2}\cdot\vec{\rho}_2} f^*(z_2) V(|\mathbf{r_1} - \mathbf{r_2}|) \frac{1}{\sqrt{A}} e^{i\mathbf{k_1}\cdot\vec{\rho}_1} f(z_1)\phi_b(\mathbf{r_2}),$$
$$(3.37)$$

where the dummy coordinates $\mathbf{r}_i = (\vec{\rho}_i, z_i), i = 1, 2$ are to be integrated out to obtain a impact ionization rate as a function of the momentum $\mathbf{k}$ of the incident hole. The integral is complicated by the entanglement of dummy variables $\mathbf{r}_1$ and $\mathbf{r}_2$ but it can be eased by replacing the Coulomb interaction with its representation in Fourier expansions

$$\frac{1}{4\pi\epsilon} \frac{e^2}{|\mathbf{r_1} - \mathbf{r_2}|} = \frac{e^2}{\epsilon} \int \frac{d^3\mathbf{q}}{(2\pi)^3} \frac{1}{q^2} e^{i\mathbf{q}\cdot\mathbf{r_1}} e^{-i\mathbf{q}\cdot\mathbf{r_2}} . \quad (3.38)$$

Similar to Eq. (3.24) the overlap between the HH1 and LH1S, the major contributions to the matrix element come from $|z| > \frac{W}{2}$. After some algebra the scattering amplitude M arrives at the expression

$$M \quad (\mathbf{k}; \mathbf{k_1}, \mathbf{k_2}) = \left\langle \mathbf{k_1}, \mathbf{k_2} \left| \frac{e^2}{r} \right| \mathbf{k}, b \right\rangle$$
$$= \frac{1}{A^{3/2}} \frac{e^2}{\epsilon} \int \frac{dq_\perp}{2\pi} \frac{1}{q_\parallel^2 + q_\perp^2} \int dz_1 |f(z_1)|^2 e^{iq_\perp z_1}$$
$$\int \quad dz_2 f^*(z_2) I(z_2, q') e^{-iq_\perp z_2} . \quad (3.39)$$

$q_\parallel = |\mathbf{k} - \mathbf{k_1}|$ and the expression for $I(z)$ is given by

$$I(z, q') = \sqrt{\frac{4\pi a^2}{b}} \int_0^\infty d\rho h(\rho) exp \left[- \left(\rho^2 + \frac{(z - z_0^\pm)^2}{b^2} \right)^{\frac{1}{2}} \right] , \quad (3.40)$$

where the function $h(\rho)$ is $\rho J_0(aq'\rho)$ for the case of HH1S as initial state and is $\sqrt{\frac{1}{2}}\rho^2 J_1(aq'\rho)$ for the case of HH2P$\pm$ as initial state. J stands for the

Bessel functions. $q' = |\mathbf{k} - \mathbf{k}_1 - \mathbf{k}_2|$ and $\chi = \sqrt{1 + a^2 q'^2}$. The upper script $\pm$ is for $z > 0$ and $z < 0$ respectively. Note that $I(z, q')$ decreases with the momentum transfer q' as a consequence of localization of the initial acceptor state. The scattering amplitude is expected to decrease rapidly when the momentum transfer q' is larger than the inverse of the Bohr radius a of the localized orbital. Hence we simplify the expression Eq. (3.36) as

$$
\begin{aligned}
w^{ip}(\mathbf{k}) &= \frac{2\pi}{\hbar} |\overline{M}|^2 \sum_{\mathbf{k}_1, \mathbf{k}_2} \Theta(\frac{1}{a} - |\mathbf{k} - \mathbf{k}_1 - \mathbf{k}_2|) \\
&\times \delta\left[\varepsilon(\mathbf{k}) - E_0 - \varepsilon(\mathbf{k}_1) - \varepsilon(\mathbf{k}_2)\right] \qquad (3.41) \\
&= \frac{2\pi}{\hbar} |\overline{M}|^2 \sigma(\mathbf{k}) .
\end{aligned}
$$

$\overline{M}$ stands for the maximum scattering amplitude which occurs when $k_1 = k_2$, and the angel between $\mathbf{k}$ and $\mathbf{k}_1$ is equal to that between $\mathbf{k}$ and $\mathbf{k}_2$. The summation in the above expression gives the effective phase space volume $\sigma(\mathbf{k})$ available for this scattering process given that the incident momentum is $\mathbf{k}$. Carrying out $\mathbf{k}_1$ and $\mathbf{k}_2$ integral one obtains

$$
\begin{aligned}
\sigma(\mathbf{k}) &= A^2 \int \frac{d^2\mathbf{k}_1}{(2\pi)^2} \frac{d^2\mathbf{k}_2}{(2\pi)^2} \Theta(\frac{1}{a} - |\mathbf{k} - \mathbf{k}_1 - \mathbf{k}_2|) \\
&\times \delta\left[\varepsilon(\mathbf{k}) - E_0 - \varepsilon(\mathbf{k}_1) - \varepsilon(\mathbf{k}_2)\right] \qquad (3.42) \\
&= \left(\frac{A}{(2\pi)^2}\right)^2 \int \frac{d^2\mathbf{u}}{2} d^2\mathbf{v} \Theta(\frac{1}{a} - u) \delta\left\{\frac{\hbar^2}{2m} \frac{1}{2} \left(|\mathbf{u} + \mathbf{k}|^2 + v^2\right) - [\varepsilon(\mathbf{k}) - E_0]\right\} \\
&= \frac{A^2}{2\pi} \frac{m}{\hbar^2} \int d^2\mathbf{u} \Theta(\frac{1}{a} - u) \Theta\left[-\frac{\hbar^2}{4m}|\mathbf{u} + \mathbf{k}|^2 + (\varepsilon(\mathbf{k}) - E_0)\right] ,
\end{aligned}
$$

where the phase space dummy variables $(\mathbf{k}_1, \mathbf{k}_2)$ was transformed into the new coordinates $(\mathbf{u}, \mathbf{v}) = (\mathbf{k}_1 + \mathbf{k}_2, \mathbf{k}_1 - \mathbf{k}_2)$ with corresponding Jacobian equals one half. After integrating out the variable $\mathbf{v}$ the evaluation of $\sigma(\mathbf{k})$ can be obtained through counting the overlapping area of one circle centered at origin with radius $1/a$ and another circle centered at $-k$ on the $\mathbf{x}$-axis with radius $\frac{\sqrt{4m[\varepsilon(\mathbf{k}) - E_0]}}{\hbar}$. The resultant rate w^{ip} is plotted in Fig. 3.3 as a function of kinetic energy $\frac{\hbar^2 k^2}{2m^*}$. The reverse process of impact ionization is Auger recombination, in which two HH1 holes collide and result in one localized hole and one HH1 hole with higher kinetic energy. Auger process must be taken into account as well.

The holes impact-ionized to the HH1 can go back to the low-lying localized states by acoustic phonon emission, i.e. the thermal recombination. The thermal recombination rate is given by[24]

29

$$w^{tr}(\mathbf{k}) = 2^{10}\pi \frac{c}{l_0} \frac{E_0^4 m^* c^2}{[\varepsilon(\mathbf{k}) + E_0]^5} a^3 \left| g(z_0^{\pm}) \right|^2 (N_{\mathbf{q}} + 1) \,, \qquad (3.43)$$

where c is the sound velocity. $N_{\mathbf{q}}$ is the number of phonon involved in the scattering and $\mathbf{q}$ is the wave vector of the phonon satisfying conservation of energy given by $q = [\varepsilon(\mathbf{k}) + E_0]/\hbar c$. l_0 is the characteristic length for acoustic phonon scattering

$$l_0 = \frac{\pi \hbar^4 \varrho}{2m^{*3}\Xi^2} \,, \qquad (3.44)$$

where ϱ and Ξ are mass density of the lattice and deformation potential as mentioned previously. The reverse process of the thermal recombination is the thermal excitation of holes in the low-lying localized states by acoustic phonon absorption.

Between the two localized levels, HH1S and HH2P$\pm$, the thermal capture/generation rates $t_{a/e}$ are given by

$$t_{a/e} = 2^{10} \frac{c}{l_0} \frac{mc^2}{\Delta\epsilon} (N_{\mathbf{q}} + \frac{1}{2} \mp \frac{1}{2}) \,. \qquad (3.45)$$

$\Delta\epsilon$ denotes the energy difference between the localized levels. The subscripts a and e indicate that these processes are accompanied by phonon absorption and phonon emission respectively.

3.2.4 Hole population in subband and lower localized acceptor states

From Section 3.2.2 we are able to deal with the non-equilibrium occupations $f_{\mathbf{k}}$ and f_2 with normalization up to an arbitrary total number of holes. Using the impact ionization and phonon emission rates we are now able to deal with the occupations in the subsystem consisting of lower localized levels and HH1. To be precise, we adopt the normalization given by Eq. (3.24) where the total hole density of subsystem consisting of LH1S and HH1 is equal to the vacancy density in HH2P$\pm$ and HH1S. Since the occupation probability f_2 is completely determined from $f_{\mathbf{k}}$, it is convenient to write the density of HH1 holes n_s as

$$n_s = \frac{n_s}{n_s + n_a f_2}(n_s + n_a f_2) = \lambda(F, T) n_a (1 - f_1 - f_g) \,, \qquad (3.46)$$

and the hole density of LH1S as
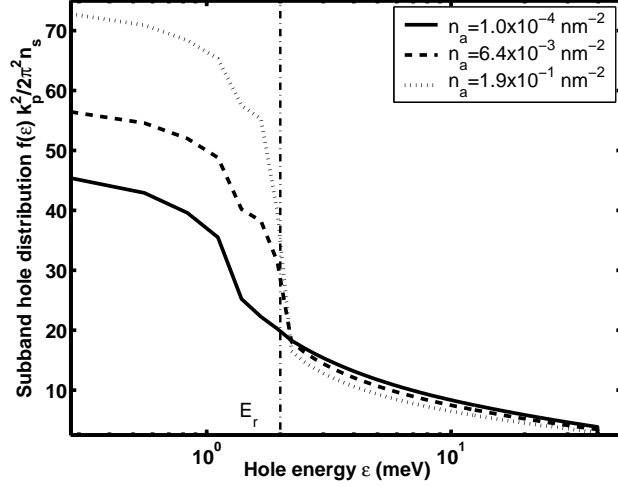
$$n_2 = [1 - \lambda(F, T)] \, n_a (1 - f_1 - f_g) \,. \qquad (3.47)$$

Figure 3.4: Normalized subband hole distribution $\tilde{f}(\varepsilon)$ versus hole energy ε for electric field strength of $F = 1000$ V/cm and $T = 1$ K. The vertical line denotes the resonance energy E_r. The distribution concentrates more in the $\varepsilon < E_r$ region as acceptor density n_a increases.

The dimensionless parameter $\lambda(F, T)$, given by Eq. (3.35), has values between zero and unity.

Once f_1 and f_g are known, f_2 can be determined from Eq. (3.47). f_1 and f_g can be calculated from the kinetics between HH1 and the low-lying localized states. Impact ionization and thermal excitation processes cause the upward transitions while Auger recombination and thermal recombination processes cause the downward transitions. The respective downward Auger recombination rates from HH1 to HH2P$\pm$ and HH1S are $r_{2p}^{ar} = A_{2p}(T)n_s^2(1-f_1)$ and $r_{1s}^{ar} = A_{1s}(T)n_s^2(1-f_g)$, where the coefficients A's are temperature- and acceptor density-dependent for the Auger recombination and the factors $(1\text{-}f_{1,g})$ account for the constraint that the process is forbidden when the lower acceptor state is filled with a hole. Note that holes in HH1 are not required to have threshold kinetic energy for the recombination process to take place, so we assume the coefficients A's have a negligible field dependence. The holes occupied the continuum can drop to the lower localized states, HH1S and HH2P$\pm$, by thermal recombination. In our case HH2P$\pm$ is below the HH1 minimum by 2 meV, which is much smaller than the gap between HH1 and HH1S, 16 meV; here we neglect the latter recombination process since the rate is inversely proportional to the gap. This downward rate from HH1 to HH2P$\pm$ is proportional to the hole density in HH1 and can be written as $r_{2p}^{tr} = C(F, T)n_s$. The coefficient $C(F, T)$, dependent on field and temperature, is
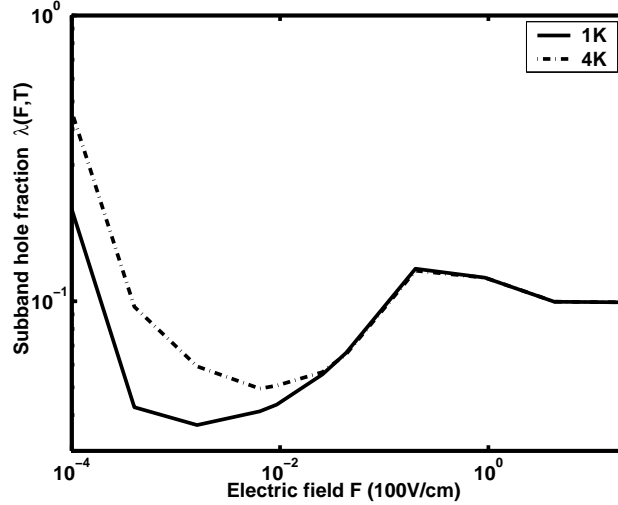
Figure 3.5: The subband hole fractions $\lambda(F,T)$ as a function of electric field F for $T = 1$ K (solid) and $T = 4$ K (dashed) are shown. The coincidence for different temperatures at higher electric fields suggests that $k_B T$ becomes irrelevant compared with the scale of E_r and optical phonon energy $\hbar\omega_0$.

taken as the average of Eq. (3.43) with respect to $f_{\mathbf{k}}$

$$C(F,T) = \frac{\sum_{\mathbf{k}} w^{tr}\left(\varepsilon(\mathbf{k})\right) f_{\mathbf{k}}}{\sum_{\mathbf{k}} f_{\mathbf{k}}} \ . \qquad (3.48)$$

We now consider upward transitions. The impact ionization rates for the respective processes, HH1S to HH1 and HH2P± to HH1, are of the expressions, $r_{1s}^{ip} = B(F,T)n_s f_g$ and $r_{2p}^{ip} = B(F,T)n_s f_1$. Note that the factors f_1 and f_g in the expressions account for the requirement of occupied initial localized acceptor state. The coefficients $B_i(F,T)$ can be written as the average

$$B_i(F,T) = \frac{\sum_{\mathbf{k}} w_i^{ip}\left(\varepsilon(\mathbf{k})\right) f_{\mathbf{k}}}{\sum_{\mathbf{k}} f_{\mathbf{k}}} \ . \qquad (3.49)$$

The subscript of w_i^{ip} in Eq. (3.49) stands for different rates resulting from different initial localized states in the different collision processes in the present case. There exists a threshold of kinetic energy for the hole in HH1 for impact ionization and consequently the coefficient B for low field and low temperature is negligibly small. Besides the upward transition caused by the inelastic collision, holes occupying the lower localized states can also be excited to the continuum through phonon emission. Here we also neglect

32

the direct excitation of HH1S holes to HH1 because it requires absorption of phonon of much greater energy. Therefore we are left with the thermal excitation from HH2P± to HH1, and the rate can be expressed as $r^{te} = D(T)n_1$. The phonon absorption coefficient $D(T)$ is determined by detailed balance with r^{tr} at thermal equilibrium.

Since we have to consider two lower localized states in the kinetic problem, we are left with the transition between HH1S and HH2P±. For simplicity we only consider the thermal excitation and recombination. The upward and downward transition among the two levels are given by $t_a n_g$ and $t_e n_1$. With all the necessary transitions at hand it is ready to write down the kinetic equations for the populations n_1 and n_g of the two localized states. Substitute all the formula into the relation we have

$$\begin{aligned}
\frac{dn_1}{dt} &- t_a n_g + t_e n_1 = r_{2p}^{ar} - r_{2p}^{ip} + r^{tr} - r^{te} \quad (3.50) \\
&= A_{2p} n_s^2 (1 - f_1) - B_{2p} n_s f_1 + C n_s - D n_1 \, . \\
\frac{dn_g}{dt} &+ t_a n_g - t_e n_1 = r_{1s}^{ar} - r_{1s}^{ip} \\
&= A_{1s} n_s^2 (1 - f_g) - B_{1s} n_s f_g \, .
\end{aligned}$$

Now we are left with the determination of the coefficients A_{1s}, A_{2p} and D which are assumed to be independent of the electric field. Since the occupations obtained from the rate equation must be restored to the thermal equilibrium when the electric field is set to zero, the requirement of detailed balance at zero field give A_{1s}, A_{2p} and D using B_{1s}, B_{2p} and C

$$\begin{aligned}
A_{2p}(T) \left(n_s^0\right)^2 (1 - f_1^0) &= B_{2p}(F = 0, T) n_s^0 f_1^0 \, , \\
A_{1s}(T) \left(n_s^0\right)^2 (1 - f_g^0) &= B_{1s}(F = 0, T) n_s^0 f_g^0 \, , \\
D(T) n_1^0 &= C(F = 0, T) n_s^0 \, . \quad (3.51)
\end{aligned}$$

Note that the zeros as upper scripts in f_g, f_1, n_1 and n_s stand for the equilibrium values.

3.3 Population inversion in quantum well resonant state laser

For given F and T, Eq. (3.50) can be solved to give f_g and f_1. Then they can be substituted to Eq. (3.47) to give f_2. $f_2/f_1 > 1$ is the condition for

population inversion. Putting everything together we are now able to obtain the non-equilibrium distribution of holes in all the levels under electric field pumping. For the subsystem containing LH1S and HH1, the normalized subband distribution $\tilde{f}(\varepsilon) \equiv f(\varepsilon)\frac{k_p^2}{(2\pi)^2 n_s}$ versus hole kinetic energy for different acceptor densities is shown in Fig. 3.4 with applied electric field 1 KV/cm. k_p stands for the hole momentum corresponding to kinetic energy of one optical phonon energy $\hbar\omega_0$=40 meV and the integration $\int_{|\mathbf{k}|<k_p} \tilde{f}(\varepsilon)d\varepsilon$ gives unity. For lower acceptor densities n_a holes in HH1 are more likely to be pumped to acquire energy exceeding resonance energy E_r. This results in lower occupation below E_r. Higher acceptor densities n_a lead to higher occupation probability at E_r, i.e. larger $\tilde{f}(E_r)$. This phenomena results from strong resonant scattering for higher acceptor densities. From Eq. (3.32) the occupation f_2 of LH1S is consequently enhanced with increasing acceptor density. In other words for same hole density in HH1, higher acceptor densities n_a lead to higher LH1S occupation probabilities f_2. Therefore higher n_a is advantageous for building population inversion. The effect of electric field is shown in Fig. 3.5 by plotting the subband hole fraction λ. At low field, the occupation of LH1S compared to that of HH1 is suppressed by the Boltzmann factor and λ is near unity. As the field is turned on (between 10^{-2} and 10^{-1} V/cm), holes acquire kinetic energy by field pumping. Hence more holes accumulate in LH1S through resonant capture of holes in HH1 with kinetic energy $\varepsilon(\mathbf{k}) = E_r$. As the field further increases, the fraction λ starts to increase because the field pumping overwhelms resonant capture and acoustic phonon scattering. In that case large fraction of holes in HH1 acquire kinetic energy larger than E_r. The temperature effect diminishes in this regime as shown by the coincidence of the two curves in Fig. 3.5. Eventually the growth of λ in the high field regime saturates when optical phonon scattering sets in.

Next we consider the subsystem consisting of HH1 and the lower localized states. At low temperature and equilibrium, most of the holes are bound by the acceptors and occupy the lowest HH1S. There are very few holes on HH1 and even fewer holes with enough kinetic energy to inelastically collide with the localized holes. Therefore the process of impact ionization is negligible, and the so is the Auger recombination because in such dilute case the average distance between the free holes is so large that the probability of collision is extremely small. Hence the populations of these levels are dominated by the thermal processes and the statistics obey the Boltzmann distribution. When the electric field is turned on, holes can acquire more kinetic energy and the impact ionization of the low-lying localized state is possible through the inelastic collisions with energetic holes. The subsequent distribution of
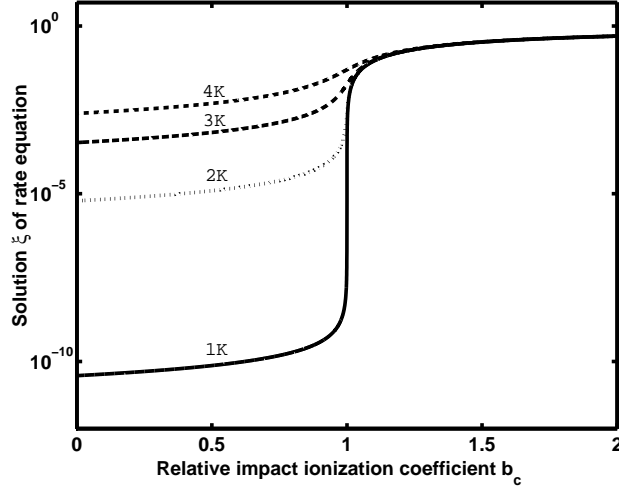
Figure 3.6: The solution ξ of equation Eq. (3.52) at low field and low temperature is shown as a function of the relative impact ionization coefficient b_c. The abrupt jump around $b_c = 1$ is due to the depletion of the lower localized levels by impact ionization.

holes are balanced by those upward and downward transitions, as illustrated in Eq. (3.50). In order to have a quantitative understanding of how electric field change the steady-state distribution of holes as the impact ionization rates increase, it is easier to consider the subsystem as HH1 and one single localized state, which is below HH1 minimum by e_g. The rate equation can be written in a similar manner, that is

$$\tilde{A}n_a\lambda^2\xi^3 + \tilde{B}\lambda\xi^2 + (\tilde{C} - \tilde{B} + \frac{\tilde{D}}{\lambda})\lambda\xi - D = 0 \,. \qquad (3.52)$$

The variable $\xi = 1 - \tilde{f}$ and $\tilde{f}$ stands for the population in the localized state. The capital letters with tildes represent the effective coefficients for the corresponding processes. Now we first focus on the limit of low temperature and low field. In such case the occupation of lower localized levels is close to unity ($\xi \ll 1$) and the impact ionization coefficient $\tilde{B}$ is nearly zero. So it is a good approximation to neglect the term of highest power in ξ in the rate equation Eq. (3.52). The solution is given by

$$\xi = \frac{(\tilde{B} - \tilde{C})\lambda + \sqrt{(\tilde{B} - \tilde{C})^2\lambda^2 + 4\lambda\tilde{B}\tilde{D}}}{2\lambda\tilde{B}} \,, \qquad (3.53)$$

where the term for thermal excitation $\tilde{D}/\lambda$ is dropped in the parenthesis

35

of Eq. (3.52) because thermal excitation process is much weaker than the thermal recombination process ($\tilde{C} \gg \frac{\tilde{D}}{\lambda}$) at low temperature. Note $\lambda \simeq 1$ at low field. In order to illustrate how electric field affects the solution ξ through impact ionization coefficient $\tilde{B}$, we set $\lambda = 1$ and define relative coefficients for impact ionization $b_c \equiv \frac{\tilde{B}}{\tilde{C}}$ and the thermal excitation $d_c \equiv \frac{\tilde{D}}{\tilde{C}}$ to the thermal recombination coefficient C. The solution can be rewritten as

$$\xi = \frac{(b_c - 1) + \sqrt{(b_c - 1)^2 + 4b_c d_c}}{2b_c} \ . \tag{3.54}$$

$d_c \simeq e^{-\beta e_g}$ is a temperature-dependent parameter in the expression as suggested by Eq. (3.51). For $b_c = 1$ ξ is $\sqrt{d_c} \ll 1$ justifying the omission the ξ^3 term in Eq. (3.52) in the regime of discussion. The relation between ξ and the relative impact ionization coefficient b_c is plotted in Fig. 3.6 for temperature from 1K to 4K. In the limit of small b_c the solution can be approximated as $\xi = d_c$ which is nothing but the thermal equilibrium. Such case corresponds to the low field situation in which the impact ionization is not yet activated. As electric field increases, b_c grows towards unity because more holes in HH1 acquire enough kinetic energy from the field. In the cross-over regime where the term $(b_c - 1)$ in Eq. (3.54) turns positive from negative, ξ grows rapidly as both the population and average kinetic energy of holes in HH1 increase. As b_c gets larger and larger than 1 the solution approaches $1 - \frac{1}{b_c}$. In the cross-over there is a competition between the two terms $(b_c - 1)^2$ and $b_c d_c$ in the square root of Eq. (3.54). Consequently the size of the cross-over is determined by $\sqrt{d_c}$. Since the impact ionization parameter b_c is strongly field-dependent, this cross-over corresponds to the variation of field δF as

$$\delta F \sim e^{-\beta \frac{e_g}{2}} \left(\frac{\partial b_c}{\partial F} \right)^{-1} \ . \tag{3.55}$$

This δF characterizes how sensitive pumping is to electric field. The dramatic jump of ξ at $b_c \simeq 1$ is due to the dominance of upward impact ionization over the downward thermal recombination. The depletion of the lower localized levels when $b_c > 1$ is critical for the realization of the hole population inversion.

After combining the two subsystem, we are able to obtain the occupation of each level in the system. The occupation probabilities f_g, f_1 and f_2 for the strain split acceptor levels and the ratio f_2/f_1 at 4K are shown in Fig. 3.7. By definition a population inversion is established if $f_2/f_1 > 1$. There is a threshold acceptor density n_a about 10^{-3} nm^{-2} when applied field is 100 V/cm. The threshold acceptor density reflects that the resonance scattering is necessary for building the population inversion. As n_a increases further, it
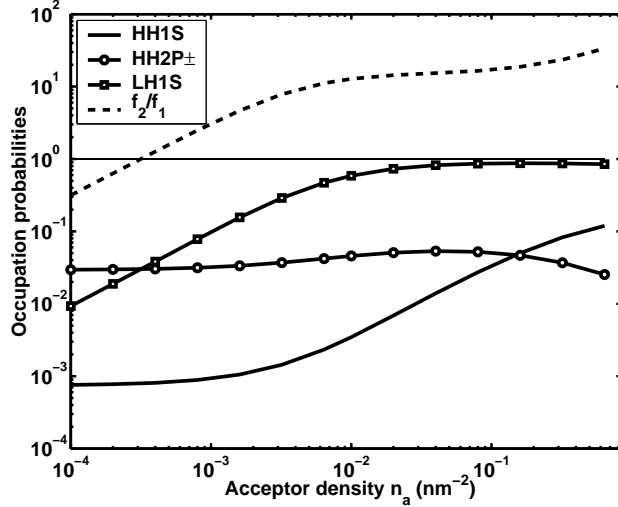
Figure 3.7: Occupation probabilities f_1 (HH2P±), f_2 (LH1S) and f_g (HH1S) for $T = 4$ K are plotted as functions of acceptor density n_a at fix electric field $F = 100$ V/cm. The population ratio f_2/f_1 is shown in solid line. The horizontal line at $f_2/f_1 = 1$ denotes that population inversion is built when n_a exceeds some threshold acceptor density.

becomes harder for HH1 holes to acquire higher energy, which is shown in Fig. 3.4, and this effect leads to suppression of the impact ionization processes from the lower levels. Even though the upward transitions get suppressed due to more resonant scattering, the population f_2 remains fixed values due to the increase of λ with increasing n_a. However this effect leads to the fact that population ratio f_g/f_1 is getting closer to its equilibrium value. For $T < 4$ K the result is the same because acoustic phonon scattering is irrelevant for low temperature and higher field. The behaviors of the system differ for low temperature ($k_BT < \delta$) and high temperature ($k_BT > \delta$) regimes. At low temperature ($T < 10$ K) population inversion can be realized for only a moderate electric field (100 V/cm) because there is almost no acoustic phonon scattering, and the hole distribution in HH1 can be easily distorted by the field. At high temperature, the distribution is stabilized by the strong acoustic phonon scattering. Therefore population inversion is impossible even for stronger field.

In Fig. 3.8 the populations of localized levels versus field strength F for $T = 10$ K are shown. As the field is turning on and increasing toward 20 V/cm, holes on HH1 become more and more energetic. Consequently more and more free holes are generated due to the increase of coefficients B_{1s}

and B_{2p}. Note that presently the resulting upward transition is mainly from HH1S to HH1 because the upper level HH2P± is empty, and the population f_1 mainly results from the combined processes, impact ionization HH1S to HH1 plus the thermal recombination from HH1 to HH2P±. As F continues to increase, the populations f_1 and f_2 grow significantly and the lowest HH1S begins to deplete due to the fact that the intra-center recombination from HH2P± to HH1S is quite slow. Now the upward transition is contributed more by HH2P± than HH1S. When the field exceeds the threshold field, 20 V/cm in our case, the lowest HH1S is almost empty and the pumping process is mainly controlled by the transitions between HH1 and HH2P±. The abruptness of the growth of f_2 is inversely proportional to the temperature according to Eq. (3.55). However the population f_2 comes to a fixed value for the field $F > 30$ V/cm. This saturation is indicative of the fact that impact ionization rates have a upper bound. If we further increase the temperature, acoustic phonon scattering and thermal recombination become important and $k_B T$ comes back as a relevant energy scale. When the thermal energy dominates the transport process, the electric field is no longer able to significantly push the distribution away from equilibrium. Based on these results we predict the optimal conditions for hole population inversion ratio f_2/f_1 are $n_a = 10^{-3}$ nm^{-2}, $F = 100$ V/cm and temperature below ten Kelvins. These conditions in a QW structure specified in Section 3.1.1, with central width $W = 11.7$ nm and Germanium compositions $x = 0.088$ and $y = 0.094$, are well within the range of experimental implementation.

3.4   Concluding Remarks

Before drawing the conclusion, some non-ideal effects have to be remarked here. In real structure there are always compensating donors present. We assume the donor density in the δ-doped region is n_d. With the presence of the compensating donors, the density of holes is reduced to be $n_a^* = n_a - n_d$ in the number normalization equation, Eq. (3.24). The presence of the donors reduces the total number of holes and increases the number of unoccupied impurity levels. Since the governing equations for the distribution of holes are nonlinear due to impact ionization and Auger recombination as shown in Eq. (3.50), the impact ionization threshold and many other properties depend on the total number of holes and therefore the compensation ratio n_d/n_a. The immediate consequence is the increase of threshold electric field for impact ionization due to fewer energetic holes generated than in the ideal case without compensating donors. However the laser threshold electric field will not be increased too much with the inevitable donors in reality. In addition two-
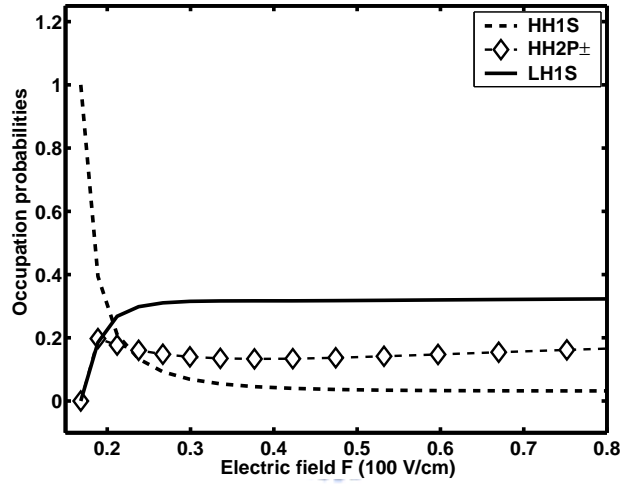
38

Figure 3.8: Occupation probabilities f_g of HH1S, f_1 of HH2P$\pm$ and f_2 of LH1S versus electric field F at T = 10 K are shown. Population inversion is achieved when the electric field is larger than 20 V/cm. As the temperature further increases, population inversion is not possible because the electric field can not drive the hole distribution significantly away from equilibrium. Therefore $T = 10$ K is the critical temperature for population inversion in our case.

level impurity interacting with a continuum employed in our model can lead to S-shaped current-field dependence and bistability when the compensating donors are present. This nonlinear behavior has been studied extensively in p-Ge[25] and for recombination-generation models in semiconductors in general.[26] It allows low and high current state for a given field. In order for our quantum well structure to achieve population inversion, the system must be in the high current state. Actually the S-shaped dependence comes from multiple solutions of the steady-state rate equation for the occupations and is independent of carrier species and systems. Hence the S-shaped dependence is expected to occur as well in our subband system if the compensation ratio n_d/n_a is too large. In summary we estimated that the effects of donors are negligible if n_d/n_a is much smaller than 0.01.[25]

In conclusion, we propose a QW structure with resonant state and show that the relative energies of the strain-split localized states and the continuous states enable laser operation with photon frequency as low as 1 THz. The hole distributions are studied in detail with considerations of all the related microscopic physical processes. Calculations on the occupation probabilities of the localized states reveal that there are thresholds for external field and acceptor density in order to achieve the population inversion. For 1 THz lasing, the required field is 100 V/cm at temperature below 10K. These conditions can be easily realized in experiments. This work leads to a new and practical direction for semiconductor THz laser with arbitrarily small radiation frequency.

Chapter 4

Appendix

4.1 Algebraic formulation of resonant state

In this appendix we give the details of the binding energy corrections to the LH1S impurity state in the presence of the QW and the off-diagonal couplings with the HH1 continuum. For simplicity the envelope functions for the localized impurity state and the QW continuum are denoted by ϕ and $\psi_{\mathbf{k}}$ respectively. The unperturbed states satisfy the equations

$$
\begin{aligned}
\left[H^0_{LK} + V_I(r) + V_C(z_0)\right]\phi\, u_{3/2} &= E_{1s}\phi\, u_{3/2}\,, \\
\left[H^0_{LK} + V_C(z)\right]\psi_{\mathbf{k}}\, u_{1/2} &= \varepsilon_{\mathbf{k}}\psi_{\mathbf{k}}\, u_{1/2}\,.
\end{aligned}
\tag{4.1}
$$

Considering the full Hamiltonian, the eigenstates are superposition of the form

$$
\Psi_p = \sum_{m=\pm\frac{1}{2}} a_p^{(m)}(\phi\, u_m) + \sum_{m=\pm\frac{3}{2}} \Sigma_{\mathbf{k}} b_{p\mathbf{k}}^{(m)}(\psi_{\mathbf{k}}\, u_m)\,.
\tag{4.2}
$$

Here the index p denotes the label for the hybridized states and it runs through the total number of continuous states plus one. Substituting the hybridized states into the equation $H\Psi_p = \epsilon_p\Psi_p$, a set of algebra equations for the coefficients a_p and $b_{p\mathbf{k}}$ are obtained.

$$
\begin{aligned}
a_p^{(\frac{1}{2})}(\epsilon_p - E_{1s} - \Delta) &= \sum_{\mathbf{k}} b_{p\mathbf{k}}^{(-\frac{3}{2})}\alpha_{\mathbf{k}} \\
b_{p\mathbf{k}}^{(-\frac{3}{2})} - \Sigma_{\mathbf{k}'}b_{p\mathbf{k}'}^{(-\frac{3}{2})}\beta_{\mathbf{k}\mathbf{k}'} &= a_p^{(\frac{1}{2})}\alpha_{\mathbf{k}}^*\,,
\end{aligned}
\tag{4.3}
$$

where

41

$$\beta_{\mathbf{kk}'} = \langle \psi_{\mathbf{k}} | v_I(r) | \psi_{\mathbf{k}'} \rangle \,. \tag{4.4}$$

$\beta_{\mathbf{kk}'}$ stands for the intraband transition due to Coulomb interaction from the impurity center. Note that we omit another set of equation for $m = -1/2$ and $m = 3/2$ because they are identical to Eq. (4.3). The eigenvalue ϵ_p can be solved by by iterative substitution from Eq. (4.3) and the leading terms are

$$\epsilon_p = E_{1s} + \Delta + \sum_{\mathbf{k}} \frac{|\alpha_{\mathbf{k}}|^2}{\epsilon_p - \varepsilon_{\mathbf{k}}} + \sum_{\mathbf{k}_1 \mathbf{k}_2} \frac{\alpha_{\mathbf{k}_1}^* \beta_{\mathbf{k}_1 \mathbf{k}_2} \alpha_{\mathbf{k}_2}}{(\epsilon_p - \varepsilon_{\mathbf{k}_1})(\epsilon_p - \varepsilon_{\mathbf{k}_2})} \,. \tag{4.5}$$
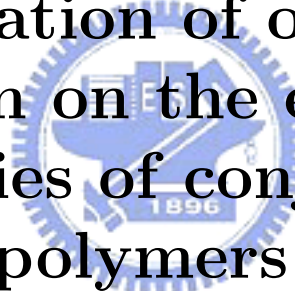
The perturbed energy for LH1S can be obtained by directly substitute the unperturbed energy E_{1s} for ϵ_p in the right hand side of Eq. (4.5). Aided by the equality $\frac{1}{x+i} = P\frac{1}{x} - i\pi\delta(x)$ to avoid the singularity and neglect the higher order terms, expressions for the shift of binding energy ΔE_{1s} and the corresponding imaginary part energy are obtained.

$$\Delta E_{1s} = \Delta + P\frac{A}{(2\pi)^2} \int d\mathbf{k} \frac{|\alpha_{\mathbf{k}}|^2}{E_{1s} - \varepsilon_{\mathbf{k}}} \,, \tag{4.6}$$

$$\frac{\Gamma_{E_{1s}}}{2} = \pi \frac{A}{(2\pi)^2} \int d\mathbf{k} \delta(E_{1s} - \varepsilon_{\mathbf{k}}) |\alpha_{\mathbf{k}}|^2 \,. \tag{4.7}$$

Part II

Implication of oxygen adsorption on the electronic properties of conjugated polymers

Chapter 5

Theoretical backgrounds for organic semiconductor physics

5.1 Hückel model for one-dimensional lattice and spontaneous symmetry breaking by phonon interaction

Organic semiconductor is a class of materials whose constitute element is carbon atom, and which have the electronic and optical properties of semiconductor, such as modulated conductivity by doping or electric field, and the absorption spectrum with a sharp edge. Conjugated polymer and small molecules belong to this category. Such materials can be made to light-emitting diodes with high efficiency due to its small dielectric constant, which in turn gives the excitions in organic semiconductors a large binding energy. Moreover, because of the large area process by spin coating, its flexible substrate and potential integration of electronic and optical applications, organic semiconductors have emerged as a candidate material for future optoelectronic applications[27]. In this thesis the focus is on the conjugated polymers.

In order to understand the fundamental principles of carrier transport, optical excitations, and quasi-particles in conjugated polymers, we shall first study its electronic structure. Most of the electronic and optical properties can be well explained from it. Since the conjugated polymers can be basically described as a long chain of repeated chemical units, such as benzene ring, the band picture is of fundamental importance for further concept development.

A single atom has its own set of discrete energy level which can be obtained by, roughly speaking, solving the the Schrödinger equation resembling

the one for an hydrogen atom. When two atoms approach each other and form a diatomic molecule, the spectrum is still a set of discrete energy levels. Taking H_2 as the simplest case, the bonding and anti-bonding combinations of $1s$ orbitals from both hydrogen atoms make up two molecular orbitals for H_2, and the respective energies are equally split from the hydrogen $1s$ level. It is true for the p and d orbitals as well. Furthermore, according to the rotational symmetry with respect to the connecting axis, we can classify the combinations into two categories, one is π category which has the odd symmetry such as p_z-p_z, while the other is σ category which has the even symmetry such as $1s$-$1s$ and p_x-p_x[28]. Moreover, the bonding orbitals always have lower energy than the corresponding anti-bonding ones since the latter contains larger kinetic energy. The σ-orbitals usually have a larger split among them because of the larger wave function overlap, which in turn causes a larger resonance integral[28]. The concept can be generalized to larger molecule or polymers which consists of numerous atoms, and their spectra evolve into a set of continuous distributions of energy levels, or a band, due to the fact that the number of levels can increase as the molecule size while the range of energy must remains a finite number which leads to more and more nearly degenerate levels.

Shown in Fig. 5.2 is the chemical structure for poly (p-phenylene vinylene) (PPV), which is a typical example of conjugated polymer. As seen from the figure, the polymer is a chain of the repeated unit consisting of a benzene ring. Each carbon connects with the adjacent carbons through the sp^2 bonding, or σ-bond, which is made up with the $2s$, $2p_x$ and $2p_y$ orbitals. In addition, the $2p_z$ orbitals between adnacent carbons can also form a chemical bond called π bond. From the band theory, the periodic σ-bonds develop a set of σ-bands while the π-bonds develop a set of π-bands. Next we are going to establish the technical part for the band theory.

We can regard the conjugated polymer as a perfectly periodic one-dimensional lattice, even though in reality the presence of disorder such as structure disorder, chemical defect, and chain end can cause some qualitative differences. For simplicity we consider the case where each unit cell contributes one state. In the tight-binding limit, the Hamiltonian is usually written as

$$H = \sum_i \left\{ \varepsilon \psi_i^\dagger \psi_i + \left[(-t) \psi_i^\dagger \psi_{i+1} + h.c. \right] \right\}, \qquad (5.1)$$

where $\psi_i^\dagger$ is the field operator creating an electron at ith site. ε and t are, respectively, the on-site energy and the coupling between adjacent unit cells. Writing the field operator in terms of its Fourier component a_k can give a diagonal Hamiltonian $\sum_k \epsilon(k) a_k^\dagger a_k$. The new set of basis,
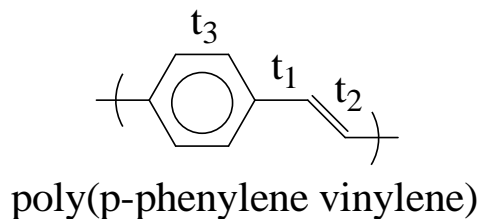
poly(p-phenylene vinylene)

Figure 5.1: Chemical structure for PPV and its tight-binding parameters.

$$a_k = \sum_i e^{ika} \psi_i \,, \qquad (5.2)$$

as a linear combination of localized atomic orbital, is delocalized throughout the whole lattice. The corresponding spectrum, given by

$$\epsilon(k) = \varepsilon - 2t \cos ka \,, \qquad (5.3)$$

is then centered at ε with bandwidth $4t$. Here we note that when each unit cell contributes one electron, then the virtual solid is a metal since the Fermi level coincides with the band and gives a finite density of state near the level. We will demonstrate later that such metallic nature of the 1D carbon lattice is not true when one considers the interaction with lattice vibrations.

The observed band gap in the spectrum for polyacetylene[29], whose basic unit cell contains only one carbon atom, proves the above consideration to be invalid. The discrepancy comes from the fact that we ignore the degree of freedom from lattice. Consider the following Hamiltonian[30]

$$H = -\sum_{i,s}(t_{i,i+1}\psi_{i+1}^{\dagger}\psi_i + h.c.) + \sum_i \frac{1}{2}K(u_i - u_{i+1})^2 + \sum_i \frac{1}{2}M\dot{u}_i^2 \,, \qquad (5.4)$$

where u_i represents the displacement of ith atom and the latter two terms stand for the lattice vibration. The coupling now is a function of adjacent displacement,

$$t_{i,i+1} = t_0 - \alpha(u_i - u_{i+1}) \qquad (5.5)$$

We first neglect the kinetic term in the Hamiltonian in the spirit of Born-Oppenheimer approximation since the mass for atom M is much larger than

electron's mass. Then one may think the u_i's are all zero in order to have the translational invariance when shifting one unit cell. Next we can think what happen if not all the u_i's are zero. For a simple case, consider the following set of displacement

$$
\begin{aligned}
u_i &= u_0 , \\
u_{i+1} &= -u_0 ,
\end{aligned} \tag{5.6}
$$

Apparently, this will increase the vibration energy as the second term in Eq. (5.4)is not zero now. However, the size of unit cell also doubles as the inclusion of Eq. (5.6), which induce a band gap and the resultant energy for total electrons is lowered. In the limit of very large K, the eventual ground state for the electron-phonon system still has the phase that all u_i's are zero to avoid the great cost for lattice vibrations. Quantitatively the vibrational energy increases as u_0^2, and the electronic energy decreases roughly as the band gap, which has a linear term in u_0. Therefore there exists a phase corresponding to a nonzero u_0 and has lowest energy[30]. The existence of such phase manifests the breaking of discrete translational symmetry, or the Pierels instability. The spectrum for the double-size unit cell can be obtained by the following Hamiltonian[31]

$$
H = \sum_n \left[(-t_+)\psi_{2n-1}^\dagger \psi_{2n} + (-t_-)\psi_{2n}^\dagger \psi_{2n+1} \right] + h.c. \tag{5.7}
$$

where

$$
\begin{aligned}
t_+ &= t_0 + \alpha u_0 \\
t_- &= t_0 - \alpha u_0 .
\end{aligned} \tag{5.8}
$$

The resultant spectrum is given by

$$
E_k^\pm = \pm\sqrt{t_+^2 + t_-^2 + 2t_+ t_- \cos 2k} . \tag{5.9}
$$

For more complicated unit cell, such as poly(p-phenylene vinylene) (PPV), similar symmetry breaking also occurs as shown by the alternative single-double bond labeled by t_1 and t_2 in Fig. 5.2. The following matrix can be diagonalized to give the π-band for PPV.
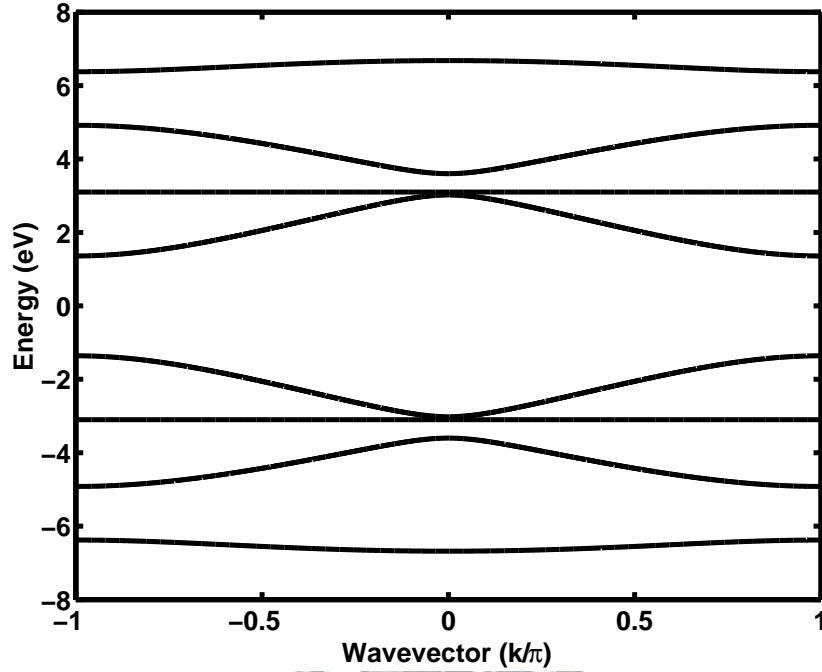
Figure 5.2: The π-bands resulting from diagonalizing the matrix in Eq. (5.10)

$$H_{PPV}(k) = \begin{pmatrix} 0 & t3 & t3 & 0 & 0 & 0 & 0 & t_1 e^{ika} \\ t3 & 0 & 0 & t3 & 0 & 0 & 0 & 0 \\ t3 & 0 & 0 & 0 & t3 & 0 & 0 & 0 \\ 0 & t3 & 0 & 0 & 0 & t3 & 0 & 0 \\ 0 & 0 & t3 & 0 & 0 & t3 & 0 & 0 \\ 0 & 0 & 0 & t3 & t3 & 0 & t1 & 0 \\ 0 & 0 & 0 & 0 & 0 & t1 & 0 & t2 \\ t_1 e^{-ika} & 0 & 0 & 0 & 0 & 0 & t2 & 0 \end{pmatrix}. \tag{5.10}$$

where t_1=-2.2 eV, t_2=-3.0 eV, and t_3=3.1 eV.

We briefly summarize the above arguments in Fig. 5.3. When neglecting the lattice vibration, the unit cell has its original size and the band is half-filled as in (a). Such a half-filled band corresponds to a metal. When considering the lattice vibration, Pierels instability occurs as in (c), which in turn develops a band gap at $k = k_F = \pi/2$, and the filled band corresponds to an insulator.
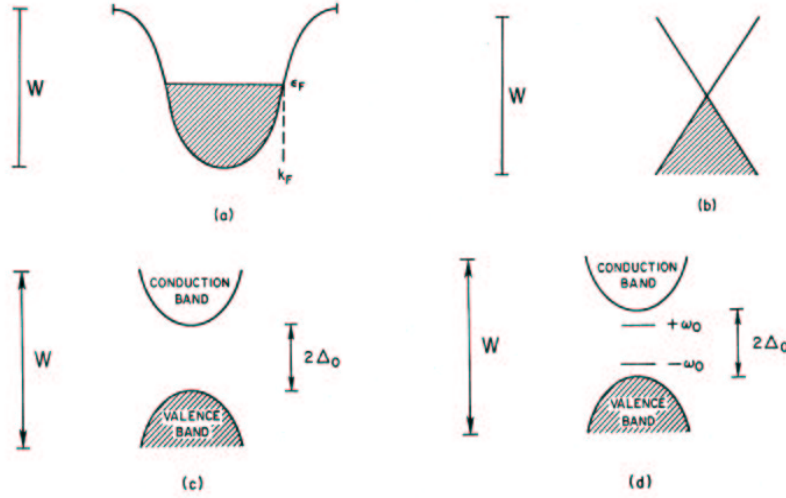
48

Figure 5.3: Various spectrum as the phonon coupling is turned on[32].

5.2 Polaron and soliton

Continuing the discussion in previous discussion, it is convenient to define a order parameter ϕ to distinguish the two different phases of the degenerate ground state.

$$\phi_i = (-1)^i u_i . \tag{5.11}$$

Under such definition, the two ground states as shown in Fig. 5.4, denoted by A and B, have the order parameter ϕ of $+u_0$ and $-u_0$ respectively. This helps our further discussion on the elementary excitation, or quasi-particle, in the phonon-coupling system.

In a band insulator, the lowest excitation is a free electron-hole pair by exciting a valence electron to the conduction band. However, in this strong phonon-coupling 1D system, the lattice degree of freedom must be taken into account when considering the excitation. Furthermore, it is the phonon coupling that there exists excitation which has energy lower than the band gap. This is where organic and inorganic semiconductors differ most.

Recalling the order parameter in Fig. 5.4 where ϕ remains a constant throughout the whole lattice. Intuitively, one can construct the excitation by the simple topological deformations such as those shown in Fig. 5.5. Actually the excitation in the left is called polaron. The spectrum can be obtained
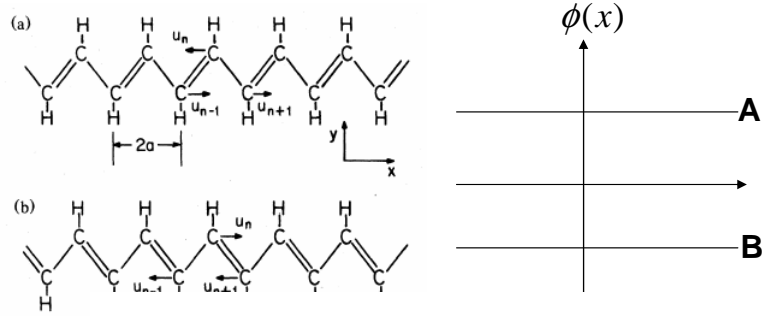
49

Figure 5.4: Con   sponding order
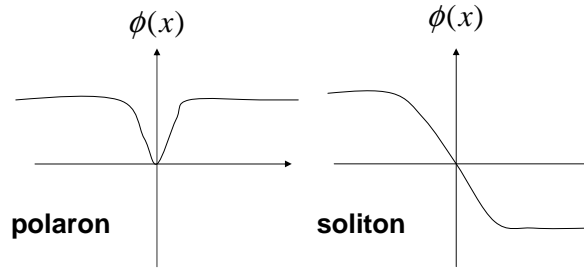parameters ϕ's.

Figure 5.5: Order parameters ϕ for polaron (left) and soliton (right).

through a trial function for the vibrational part which contains a variational width for the deformation. The resultant energy levels with two additional gap states are shown in (d) of Fig. 5.3. The gap states, corresponding to the polaron states, are of crucial importance when one considers the injection of carrier into the polymer. The excess charge carriers are stored in the polaron state instead of the conduction or valence bands in rigid semiconductors.

On the other hand, the right in Fig. 5.5 represents an soliton excitation. Soliton is unique in that the deformation leads to the formation of an electronic state near the center of band gap. For zero occupance, however, the chain is positively charge but has no net spin. Similarly for the double occupance, the chain is negatively charge and of no net spin. The state of single occupance is neutral but with a net spin 1/2, which is in great contrast to

50

the free electron.

5.3 Excition and the quantum yield in light-emitting polymers

Exciton is an excitation for a quasi-bound state consisting of a pair of electron and hole in which there is a Coulomb attraction between them. Such excitation has an energy lower than a free pair of electron and hole which has the energy larger than the band gap. The existence of such excitation will correct the ideal absorption spectrum of a semiconductor in which the minimum excitation energy is the band gap. In addition to the sharp edge associated with a band-to-band transition, the exciton can induce an absorption below the sharp edge.

The equation of motion for the quasi-bound state can be decomposed into two parts; one is a free Hamiltonian in the center of mass frame, while the other is for the relative motion. The latter has a Hamiltonian resembling the hydrogen atom and is responsible for the binding energy. Since the dielectric constant in conjugated polymers is usually much smaller (about 3) than that in inorganic semiconductors (about 10), the exciton in conjugated polymers usually has a small Bohr radius and a large binding energy. The reason for the small dielectric constant may result from the smaller size of carbon atoms relative to the silicon atoms, which makes carbon atoms more difficult to be polarized.

In the frame of relative motion, the spatial wave functions for the bound states can be classified according to the rotational symmetry. However, the Fermi statistics must be taken into account in order to have the correct product of spatial and spin wave functions. For the pair of spin singlet configuration, the lowest state has s-wave symmetry. For the pair of triplet spin, then the lowest state has p-wave symmetry. As shown in Fig. 5.6, S_1 is the lowest exciton state for spin singlet and T_1 is the lowest for spin triplet. Note that S_1 is the lowest among all exciton excitation because S_1 has the smallest Bohr radius and the largest binding energy.

The operation of a light-emitting polymers has much to do with the energy diagram in Fig. 5.6. Electron and hole can be injected into the light-emitting layer, forming exciton and then decaying into the ground state with emitting a photon. However, the ground state labeled by S_0 is nondegenerate and has zero spin component. Since the electromagnetic interaction responsible for the decay, actually the operator A·P, does not contain operators which can flip the spin, only the spin singlet exciton S_1 can decay into the ground state
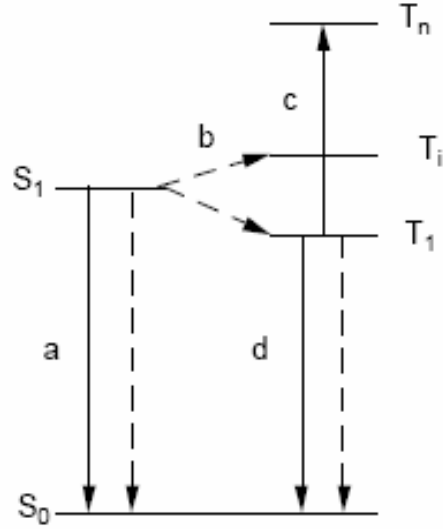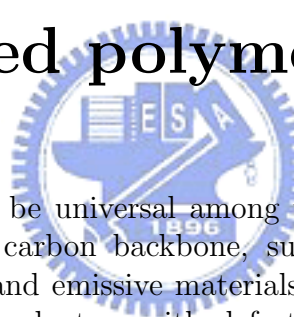
Figure 5.6: Energy diagram for spin-singlet, labeled by S, and spin-triplet, labeled by T, excitons[27].

without further assistance such as phonon. Consequently only the fraction of pairs which forms spin singlet can contribute to the emitting process. Hence the internal electroluminescence (EL) quantum efficiency η_{int} for a typical LED can be written as a product $\gamma\eta_s q$ where γ is the exciton formation ratio per injected pair, η_s is the recombination branching ratio through the spin singlet, and q is the singlet exciton radiative decay probability. In fact, q can be close to unity while γ is improved by using multilayer structure. Therefore η_s can be taken as the intrinsic yield that sets the theoretical limit for η_{int}.

Chapter 6

The unbalancing effect of adsorbed oxygen molecules on electron versus hole transport in conjugated polymers

Adsorption of O_2 seems to be universal among the organic semiconductor based on the sp^2-bonding carbon backbone, such as polythiophene, carbon nanotube, pentacene, and emissive materials for organic light-emitting diodes. For organic semiconductors with defects, the O_2 can worsen the transport for electron by forming a hybridized state with the electron trap, which will bind the electron more tightly. Under such circumstance, the electron mobility can be much smaller than the hole mobility, which is usually observed for a large class of conjugated polymers and small molecules.

In this chapter the generally observed higher hole mobility relative to electron mobility in conjugated polymers is explained with the defects and adsorbed molecular oxygen. Adsorption of the extrinsic molecular oxygen leads to that electrons are bound more tightly than holes by the traps in the originally symmetric electronic system. Hence the mobility imbalance emerges from the asymmetric binding energies. Besides, the defects are the favored adsorption sites because the intermolecular attraction is enhanced due to stronger induced dipole-dipole interaction when gap defect levels appear.

6.1 Overview of experimental findings on the unbalancing carrier mobility

Despite of similar effective masses[34], the hole mobility is generally several orders of magnitude higher than the electron mobility in organic semiconductors, including conjugated polymers and small molecules[35, 36, 37]. Poly(2-methoxy,5-(2'-ethyl-hexoxy)-p-phenylene vinylene) (MEH-PPV) and pentacene are typical examples of such imbalance[36, 37]. Transport measurements and comparisons with theoretical models suggest there are much more electron traps than hole traps[38, 39]. The asymmetry of traps could result from extrinsic effects like the unintentional background p-doping by chemical impurities or other chemical defects[40]. In reality mobility imbalance, however, persists even for samples with high purity. In this work we demonstrate that the ubiquitous molecular oxygen is the ultimate entity which breaks the electron-hole symmetry even without any chemical reaction. The highest occupied orbital of O_2 is half-filled and ready to partially accept an electron from the organic semiconductor once physically adsorbed. Our calculation shows that the electronic structures of the originally symmetric defects are significantly altered by the physically adsorbed O_2, and the trap binding energy for electron becomes much larger than holes. Difference in binding energy naturally leads to imbalanced carrier mobilities. The huge mobility difference is a consequence of the presence of traps and the adsorption of O_2, thus the idea can be generalized to all the disorder organic semiconductors. To be specific, we investigate the carrier excitations in π-conjugated poly(p-phenylene vinylene) (PPV) chain whose backbone contains a single defect which leads to two gap energy levels. The conduction for electron and hole are supposed to be completely the same because the two emerging defect levels are symmetric. However this symmetry is broken when O_2 is close to the defect and provide a pathway only for the electron in the anti-bonding polymer defect level. The asymmetry results in larger binding energy for trapped electrons than that for trapped hole by a few hundreds of meV. Transport model shows that the mobility can be made different by 2-3 orders of magnitude at high adsorption density. Since no chemical reaction takes place, this effect is reversible once oxygen is removed.
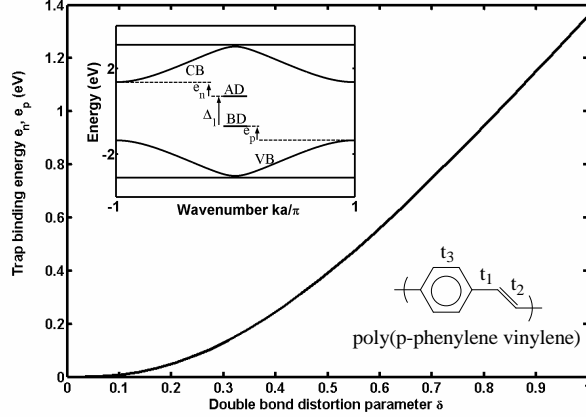
Figure 6.1: Shown in the right inset is the chemical structure for PPV as well as its tight-binding parameters t's. The left inset shows the schematic band structure of the PPV chain with one defect unit. See the text for the details of the levels.

6.2 Electronic structure for defect levels in conjugated polymers

The inset of Fig. 6.1 shows the chemical structure for a perfect PPV chain. Adopting the resonance integrals of t_1=-2.2 eV, t_2=-3.0 eV, and t_3=-3.1 eV one can fit the valence and conduction band structures obtained by more sophisticated computations[40]. The defect levels appearing in the gap can be obtained by introducing a one-bond defect in one single repeat unit with all other units remaining perfect. For PPV, defect levels can be caused by the reduction of the vinyl double-bond t_2 due to structure distortion[40]. The electronic structure is shown schematically in the inset of Fig. 6.1 where CB and VB respectively denote the conduction and valence bands, and the band gap for perfect chain is E_g =2.8 eV. The defect levels labeled by AD and BD refer to the fact that their corresponding wavefunctions have anti-bonding and bonding symmetry with respect to the center of the reduced double-bond. Now the BD and AD are, respectively, the the highest occupied molecular orbital (HOMO) and the lowest unoccupied molecular orbital (LUMO). Their difference is designated by Δ_1. The energy gaps e_n and e_p stand for binding energies for the trapped electron and hole respectively. e_n=e_p is guaranteed by the electron-hole symmetry. Denoting $t_2' = t_2(1 - \delta)$ for the reduced double-bond, the equal binding energies are plotted as a

function of δ in Fig. 6.1. It can be seen that as δ increases toward unity, the binding energies increase and their wavefunctions become more localized around the reduced double-bond. Below we discuss how the presence of oxygen alters this symmetric picture.

6.3 Electronic configuration for oxygen molecule and the intermolecular force

It was suggested that O_2 and PPV can form reversible charge transfer complex[41], and the probable adsorption site is the carbon-carbon double bond[42]. In fact, the band edge Bloch state wavefunction has a major contribution from the vinyl double bond. Therefore we expect that O_2 can adsorb onto the PPV chain as shown in Fig. 6.2. The empirical Lennard-Jones 6-12 potential[43]

$$V_{LJ} = \frac{A}{d^{12}} - \frac{B}{d^6},$$
(6.1)

is adopted to describe the intermolecular interaction between polymer and oxygen for separation d. The potential minimum E_0 and the corresponding separation d are given by $A = E_0 d^{12}$ and $B = 2E_0 d^6$. The minus term is due to induced dipole-dipole interaction[44]. Based on the second order perturbation, we assume B only depends on energy difference between ground state and the lowest excited state of the two-molecule system. The lowest excited state is that one electron is excited from BD to AD in PPV and one electron is excited from π to the singly occupied π^* in oxygen. Such state has energy higher than ground state by $\Delta_1 + \Delta_2$. Consequently

$$B = \frac{\alpha}{\Delta_1 + \Delta_2}.$$
(6.2)

Δ_2 in O_2 is determined by the gap between π and π^* which gives 4.35 eV[45]. α is roughly the same for all oxygen-conjugated carbon system. Coefficient A for the short-ranged repulsion is also assumed to depend only on the local atomic arrangement. Since the intermolecular interactions between carbon nanotubes and oxygen have been studied extensively[46], we can determine our unknown coefficients from them. The separation d and potential minimum E_0 have been reported to be 2.7 Å and 0.25 eV using *ab inito* calculation[46]. Then A and B are 37500 (eV-Å^{12}) and 193.7 (eV-Å^6), respectively. α=1046 (eV^2-Å^6) is obtained by the π-band gap of 1 eV in carbon nanotube. The resultant separation and potential minimum for perfect PPV-O_2 system is 2.8 Å and 0.14 eV using Δ_1=2.8 eV. With defect, the attraction coefficient is larger due to the reduced HOMO-LUMO
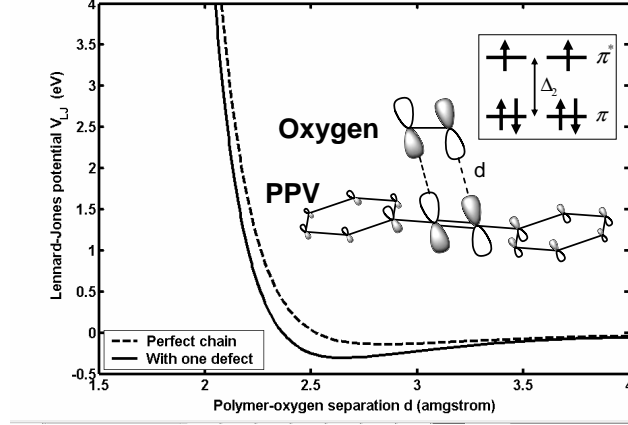
Figure 6.2: The Lennard-Jones potential between PPV chain and O_2. The dashed and the solid lines are for perfect and defect chain respectively. Also shown is the geometry for adsorption and the MOs for the oxygen π^* level and the localized AD level. The box inset gives the ground state electronic configuration for O_2 in which the energy Δ_2 represents the difference between π and π^* MOs. The gray and white indicate the negative and positive lobes of the atomic orbitals.

energy difference. Consider the case for δ=0.9 corresponding to Δ_1=0.4 eV. As shown in Fig. 6.2, the attraction is enhanced for the chain with one defect and the corresponding d=2.66 Å and E_0=0.30 eV. It is therefore energetically favorable for the molecular oxygen to be adsorbed onto the defect sites.

The Hamiltonian H for such a system is

$$H = H_p + H_o + H_{po}. \tag{6.3}$$

H_{po} stands for the interaction. For isolated PPV,

$$H_p = \sum_{n,k,\sigma} \epsilon_{n,k} b^\dagger_{nk\sigma} b_{nk\sigma} + \sum_{\alpha=\pm,\sigma} \epsilon_\alpha b^\dagger_{\alpha\sigma} b_{\alpha\sigma}. \tag{6.4}$$

σ and k are spin and momentum index respectively. $\epsilon_{n,k}$ is the n-th band energy. The subscripts $\pm$, respectively, stand for BD and AD levels and with corresponding energies $\epsilon_\pm$. For O_2, H_o must possess the property of spin-triplet ground state as well as the large on-site repulsion responding for the large difference between electron affinity (EA 0.45 eV) and ionization potential (IP 12 eV) in its gas phase[47]. If we denote the degenerate π^* orbitals in O_2 as π^*_x and π^*_z, the Hamiltonian can be written as

$$H_o = \sum_{\alpha=\{x,z\}\sigma} \left(\xi a_{\alpha\sigma}^\dagger a_{\alpha\sigma} + \frac{U}{2} n_{\alpha\sigma} n_{\alpha-\sigma} \right) - \frac{J}{2} \vec{S}_{\pi_x^*} \cdot \vec{S}_{\pi_z^*} , \qquad (6.5)$$

where ξ means the energy for the two degenerate levels and $a^\dagger(a)$ are the corresponding creating(annihilating) operators. U is the direct Coulomb repulsion when two electrons occupy the same orbital, and the positive J describes the exchange effect between the degenerate orbitals. The energy lowering by the exchange effect manifests the more stable spin triplet $^3O_2$ than the singlet $^1O_2$. The vector operator $\vec{S}$ is the total spin on each degenerate orbital. The values for U and J can be obtained by definitions of EA and IP : $(2\xi - \frac{J}{2}) + \text{IP} = \xi$ and $(3\xi + U) + \text{EA} = 2\xi - \frac{J}{2}$. ξ is O_2^+ energy and $2\xi - \frac{J}{2}$ is the $^3O_2$ energy. $3\xi + U$ is the energy for O_2^-. J is about 1 eV[46]. Hence the repulsion $U=\text{IP}-\text{EA}-J = 10.6$ eV.

6.4 Asymmetric binding energies for the trapper carriers emerging from the symmetric electronic system

Hybridization between two molecular orbitals (MO) of different symmetry is zero. Therefore the O_2 π_x^* orbital is not involved in the hybridization. Furthermore BD and all the valence band states can not hybridize with the O_2 π_z^* either since they have different parity symmetry with respect to the plane vertically cut the center of the reduced double-bond and center of internuclear line of oxygen. Consequently O_2 orbital can only hybrid with AD and the conduction band states. However the conduction band states are negligible since their MOs are extended and have relatively little components on the sites near the oxygen. Keeping the only term gives

$$H_{po} = -t \left(a_z^\dagger b_- + b_-^\dagger a_z \right) . \qquad (6.6)$$

The spin indices are neglected. The value of t can be determined from the resonance integrals β_{CO} between individual carbon and oxygen atoms. Namely

$$t = \frac{1}{\sqrt{2}}(c_1 - c_2)\beta_{CO} . \qquad (6.7)$$

c_1 and c_2 stand for the MO components of AD on the two carbon atoms defining the reduced double-bond. The resonance integral β_{CO} between the oxygen and carbon p_z separated by a distance d can be expressed as
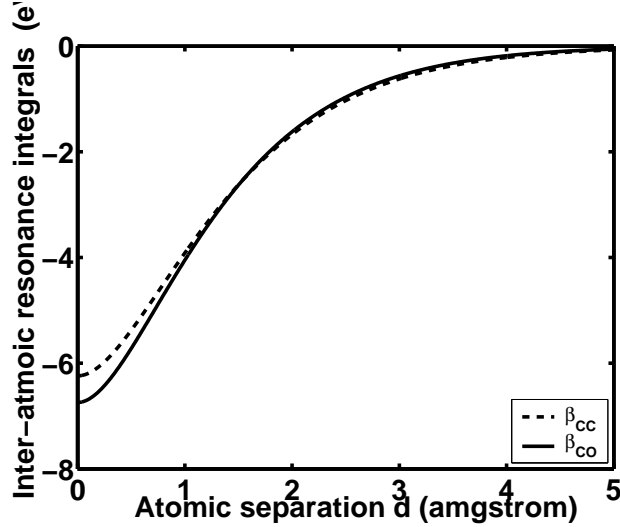
Figure 6.3: Resonance integral $\beta(d)$ is plotted as a function of separation between atoms.

$$\beta(d) = \frac{1}{4\pi\epsilon} \int d^3\mathbf{r} \varphi(\mathbf{r})\frac{1}{r}\phi(|\mathbf{r} - \mathbf{d}|) . \tag{6.8}$$

The wavefunctions φ and ϕ stand for the respective p_z atomic orbitals on carbon and oxygen atoms. The resultant β_{CO} can be simplified if one approximates the atomic orbitals as s-orbital with effective Bohr radius r_C of 0.77 Å and r_O of 0.65 Å respectively.[47]. The dielectric constant is chosen to reproduce β_{CC} used in the tight-binding model. As shown in Fig. 6.3 when d equals the single bond length 1.4 Å, β_{CC} is about -3 eV, consistent with the values commonly used for conjugated polymers. The integrals drop exponentially as d further increases. For the given Bohr radius a_1 and a_2 for carbon and oxygen atoms, the explicit form of β is given by

$$\beta(d) = \frac{\sqrt{a_1 a_2}}{\pi\epsilon d(a_1^2 - a_2^2)} \left[e^{-d/a_1}d(a_1^2 - a_2^2) + 2a_1 a_2^2(e^{-d/a_2} - e^{-d/a_1}) \right] \tag{6.9}$$

Even though a full electron transfer from polymer to oxygen is inhibited by the large repulsion energy U, the mixing of a small charge-transfer component into the ground state is enough to break the binding energy symmetry. Fig. 6.4(a) shows the ground state, denoted by $|G; n\rangle$, for the neutral system. For later convenience we set this configuration as reference, that is $\langle G; n|H_p + H_o|G; n\rangle = 0$. The one-hole configurations in Fig. 6.4(b) and (c)
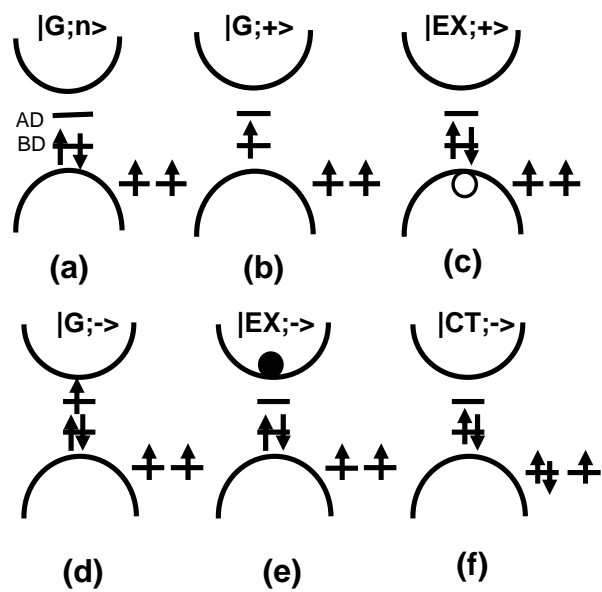
59

Figure 6.4: Electronic configurations for one extra electron and one extra hole in the hybrid system. See the text for the details of the states. Note there is no charge-transfer component for hole.

respectively stand for the trapped-hole ground state and the lowest free hole state where the hole occupies the valence band minimum. They are labeled by $|G;+\rangle$ and $|EX;+\rangle$. The matrix elements of H within this subspace is simply

$$\begin{pmatrix} \epsilon_+ & 0 \\ 0 & E_v \end{pmatrix} \tag{6.10}$$

where E_v denotes the hole energy for valence band minimum. Note that we exclude the configuration in which the the last electron in BD for $|G;+\rangle$ is transferred to oxygen, because such configuration has very high energy due to the mutual Coulomb repulsion between the two localized holes[43]. Even such state is considered, it is irrelevant since H_{po} does not contain hopping between BD and oxygen. Consequently the excitation for hole to free continuum takes energy of $E_v - \epsilon_+ = e_p$, which is the same as the O_2-free case. The situation for one electron is very different. Fig. 6.4(d), (e), and (f) denote the trapped-electron ground state, free electron state, and the charge-transfer state. They are labeled as $|G;-\rangle$, $|EX;-\rangle$ and $|CT;-\rangle$. The matrix elements for H within the three-state subspace is

$$\begin{pmatrix} \epsilon_- & 0 & -t \\ 0 & E_c & 0 \\ -t & 0 & -EA \end{pmatrix}, \tag{6.11}$$

where E_c is the energy for the conduction band minimum. The diagonal energy for charge-transfer state is $\xi + U + J/2$ and we replace it with $-EA$ by definition. Without the hopping term t the 3×3 matrix is reduced to a 2×2 one with exact symmetry to the hole problem. The point here is the ground state energy is shifted when the hopping term is involved. The ground state energy is given by

$$(\epsilon_- - EA)/2 - \sqrt{t^2 + [(EA + \epsilon_-)/2]^2} . \tag{6.12}$$

The energy of the free electron state $|EX;-\rangle$ is unaffected by t. Therefore the extra electron in the ground state is bound more tightly when the adsorbed O_2 appears. The resultant binding energy for trapped electron is larger than that for trapped hole, and the difference Δ_b versus various EA of oxygen and coupling t is shown in Fig. 6.5. The lowering of the ground state energy comes from the stabilization due to the resonance between the trapped state and the charge-transfer state. Experimentally, such lowering had been observed from the increase of the activation energy of electron trap and its level filling in MEH-PPV by exposing to air[48]. The true ground state becomes a superposition of $|G;-\rangle$ and $|CT;-\rangle$. The absolute square of
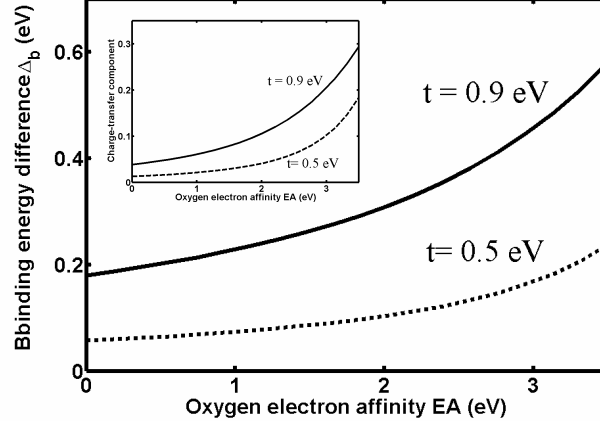
Figure 6.5: Binding energy difference Δ_b between trapped electron and trapped hole for $\delta=0.8$ is plotted for various carbon-oxygen coupling t and EA of oxygen. The larger binding energy for trapped electron is the origin for the mobility imbalance. Shown in the inset is charge-transfer component in the true ground state for one electron.

the coefficient for $|CT;-\rangle$ is also shown in the inset of Fig. 6.5. As expected the asymmetry becomes more apparent for stronger coupling t when separation d is shorter. Reduced repulsion U or larger EA in O_2 also enhances the charge transfer and the asymmetry. Actually the value of EA in solids may be higher than gas phase value due to polarization effects and structural relaxation[49]. Consider the trap binding energy of 1.0 eV corresponding to $\delta=0.8$. Choosing oxygen EA as the gas phase value of 0.45 eV, the binding energy is 1.16 eV for trapped electron and 1.0 eV for trapped hole. Indeed the electron binding energy is 0.16 eV higher. The difference is close to the deep levels measurements for MEH-PPV[50], in which the trap levels AF1 and DF1 have binding energy of 1.0 eV and 1.3 eV respectively.

Now we use the asymmetric binding energies to quantitatively explain the mobility imbalance. The carrier mobility μ in the disorder organic semiconductor depends on the number of trapped carrier n_T and free carriers n_F, and it can be expressed as[40]

$$\mu_n = \mu_{PF}/(1 + \frac{n_T}{n_F}). \tag{6.13}$$

μ_{PF} is the free polaron mobility which follows the Poole-Frenkel laws. In the case without any doping, the population ratio $\frac{n_T}{n_F}$ at low field is determined by the trap density x_t per repeat unit and the binding energies e_n and e_p.
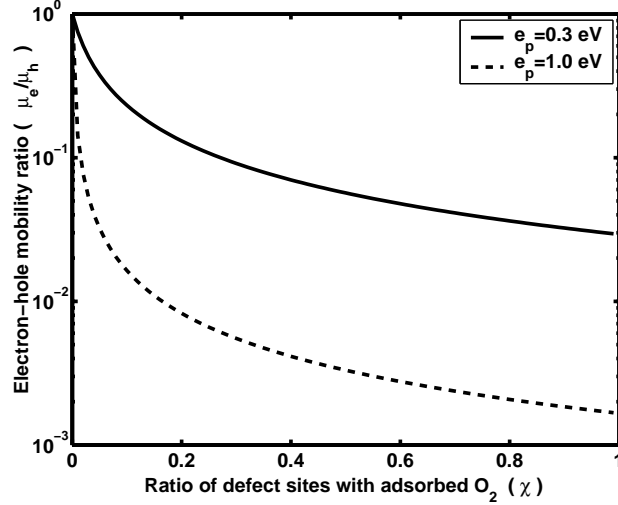
Figure 6.6: The ratio μ_e/μ_h of electron-hole mobility versus the ratio χ of defect sites which have adsorbed O_2. As χ increase, or more O_2 adsorbed onto the defect sites, the degree of mobility imbalance increases. The asymmetric effect is more apparent for trap with larger binding energy.

Thus, the electron-hole mobility ratio can be expressed as

$$\frac{\mu_e}{\mu_h} = \frac{x_t + e^{-\beta e_p}}{x_t(1-\chi) + x_t \chi e^{\beta \Delta_b} + e^{-\beta e_p}} , \qquad (6.14)$$

where χ represents the ratio of the defect sites with an O_2 adsorbed on it. Consider the case for symmetric binding energy of 0.3 eV. The resultant separation d and coupling t are 2.79 Å and 0.8 eV, which leads to electron binding energy e_n 0.4 eV and the unchanged hole binding energy e_p 0.3 eV. Assume each defect site now has an additional oxygen molecule adsorbed on it, or simply $\chi=1$. If the trap density $x_t=10^{-5}$, then the electron mobility is about 1/50 of the hole mobility, which is close to the experiment[36]. Fig. 6.6 shows the mobility ratio μ_e/μ_h as a function of O_2 adsorption ratio χ according to Eq. (6.14). The mobility imbalance is stronger as more O_2 are adsorbed onto the defect sites.

6.5   Concluding remarks

We would like to remark that the symmetry in Fig. 6.2 may be broken in reality and the oxygen bond might not be aligned with the carbon double bond. However even for the O_2 adsorbed in configurations which enable

63

the tunneling to the BD level, the hole binding energy will not be increased by the perturbation of O_2 because of the high energy cost for the hole to be transferred to O_2, i.e. the large IP of O_2. On the other hand the electron binding energy will always increase by mixing with the electron-tranfer state. Furthermore energy consideration suggests that the absorption with high symmetry is the preferred configuration. Even through many other less symmetrical configurations may be present in reality, such preferred symmetrical adsorption alone is enough to explain the electron-hole imbalance. Even though PPV is taken as the model for calculations, obviously the consideration can be extended to all organic semiconductors in which the traps and adsorbed O_2 dominate the carrier transport[35, 51, 52]. O_2 adsorption is believed to be the common origin for the carrier imbalance for polymer, small molecules, and perhaps even carbon nanotubes and fullerenes.

In conclusion the presence of localized defect levels in the gap can enhance the intermolecular attraction. The originally symmetric electronic defect structure results in huge mobility imbalance by the symmetry-breaking coupling with adsorbed O_2.

Chapter 7

The p-doping by oxygen molecules in organic semiconductors

In addition to the unbalancing effect on carrier transport in previous chapter, the adsorbed gas molecules can have a p-doping effect such that the insulating organic materials can have some free hole carriers at thermal equilibrium. Such effect can cause the OFF-state conduction and degrades the field effect transistor's characteristics by lowering its on-off ratio. From the perspective of fundamental principle, the doping by O_2 is quite different from that in conventional inorganic semiconductors where each impurity can contribute one carrier individually at room temperature. The O_2 doping, on the other hand, has a strong dependence on the dopant concentration and does not need any additional excitation in some conjugated polymers. Besides, photons of visible light wavelength can induce more carriers as well by the charge-transfer excitation.

In this chapter we investigate the sensitive effect of O_2 adsorption on the electronic properties of organic semiconductors by studying the band structures of the oxygenated system. The band structure for the O_2-adsorbed polythiophene, as an important example, is obtained by a self-consistent tight-binding scheme which takes into account the correlation effect resulting from strong Coulomb repulsion on the oxygen orbital. The adsorbed gas molecules can actually p-dope the host materials even without illumination, i.e. a ground state property. Because of the hybridization of the oxygen and polymer wave functions, the Fermi level of the oxygenated system will be pinned at the nearly half-filled oxygen band with overlap with the polymer valence band. We compare with different chemical and electronic structures for polythiophene structures and find that the doping depends critically on
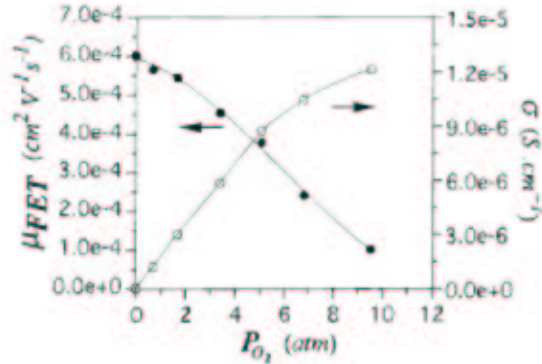
Figure 7.1: Increased conductivity and decreased carrier mobility found in P3HT FET after it is exposed to air[53].

the ionization potential. On average each oxygen molecule can dope more than 0.1 hole in dark. Furthermore, a charge-transfer excitation at about 2.3 eV photon energy to give highly mobile holes is predicted for the oxygenated system.

7.1 Overview of the p-doping in organic semiconductors

Recently the high sensitivity of electronic properties of organic semiconductors to air exposure has drawn a great deal of intention. For example, a reversible increase of conductivity, as shown in Fig. 7.1, is found in poly(3-hexyl thiophene) (P3HT) field-effect transistors (FET) after oxygen exposure during the sample preparation[53]. From the perspective of application, the oxygen exposure causes the off-state conduction in P3HT FET's and degrades the device characteristics[54, 55]. However, the off-current can be significantly reduced after placing the devices in vacuum for a few days, which suggests no chemical reaction ever took place. In addition to conjugated polymers, small molecules such as pentacene also have the similarly sensitive properties[55]. Single-wall carbon nanotubes, on the other hand, can possess alternatively n-type and p-type behaviors by switching the nanotubes in the conditions between vacuum and air exposure[56]. So far it is well accepted that such modulation is a consequence of O_2 physical adsorption which somehow induce a p-doping to the organic semiconductors. However, whether the

adsorbed O_2 results in a bulk p-doping effect[54, 55, 56] or modify the barrier between the contact[57] remains unsettled.

The p-doping process, in which electrons are removed from the host, is not clearly understood so far. From energy conservation, it appears that such process could be accomplished only with some additional energy since the ionization potential (IP) of organic semiconductors (between 5 and 6 eV) is usually much larger than the electron affinity (EA) of O_2 (0.45 eV in gas phase[59]). Indeed, as shown in Fig. 7.2, the effect of p-doping in pentacene FET is apparent only with illumination of UV light[55]. However, it does not seem so in the case of P3HT as the current-voltage measurement in dark condition still presents significant off-current[54, 55]. Besides, using poly(3',4'-dialkyl-2,2';5',2"-terthiophene) (PTT) with similar chemical structure but of larger IP, as active layer can reduce the undesired off-current to some extent[60]. Thus the p-doping can happen in dark, i.e. a ground state rather than excited state property, depending critically on the highest occupied molecular orbital (HOMO) level of the host material.

In this chapter we clarify theoretically the mechanism of p-doping in organic semiconductors for both in dark and under illumination. With a self-consistent tight-binding scheme which considers the correlation effects on O_2, we can obtain the band structures for a class of oxygenated polythiophene. Molecular oxygen is unique in that it has two half-filled molecular orbitals which contribute to its paramagnetism. Through the hybridization betweem oxygen and the polymer, the oxygen band becomes degenerate with the polymer valence band and the Fermi level is pinned by the oxygen band to lie inside the valence band. In other words, the adsorbed oxygen transform the semiconducting polymer into a metal even at the ground state. Such metal-insulator transition has been predicted for oxygenated single-wall carbon nanotube[46, 61].

7.2 Metal-insulator transition in the oxygenated single-wall carbon nanotube

Carbon nanotubes are common with most organic semiconductors, like pentacene, P3HT, and emissive materials for organic light-emitting diodes in their sp^2-bonding carbon backbone. Carbon nanotubes can have different electronic properties according to their tube chirality and diameter. Because of their size, large area surface area, and hollow geometry, carbon nanotubes are being considered as prime materials for gas adsorption. Recently there have been extensively studies on the adsorption of oxygen molecules onto
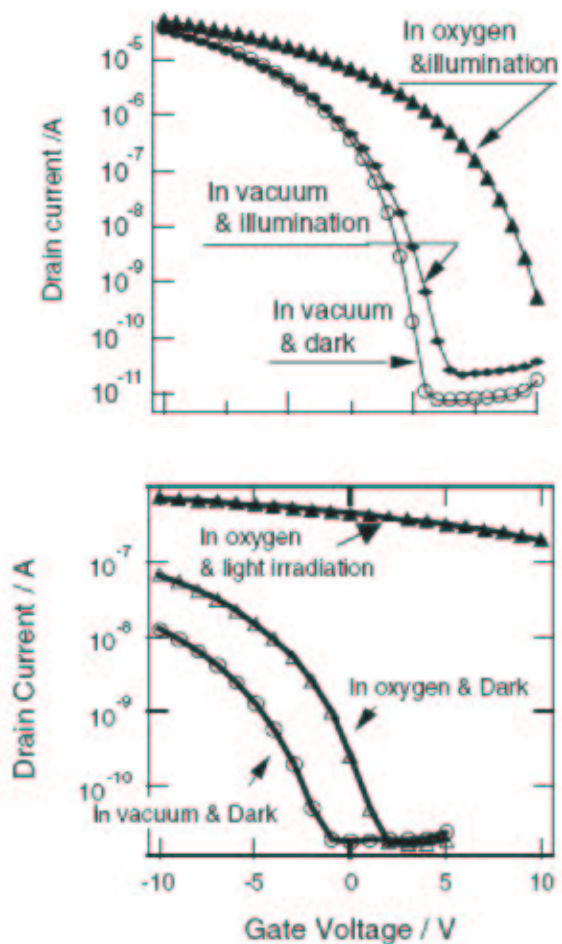
Figure 7.2: Device characteristics for pentacene FET (upper) and P3HT
FET (below) for various exposing and illuminating conditions. The pen-
tacene FET has apparent p-doping effect with both oxygen exposure and
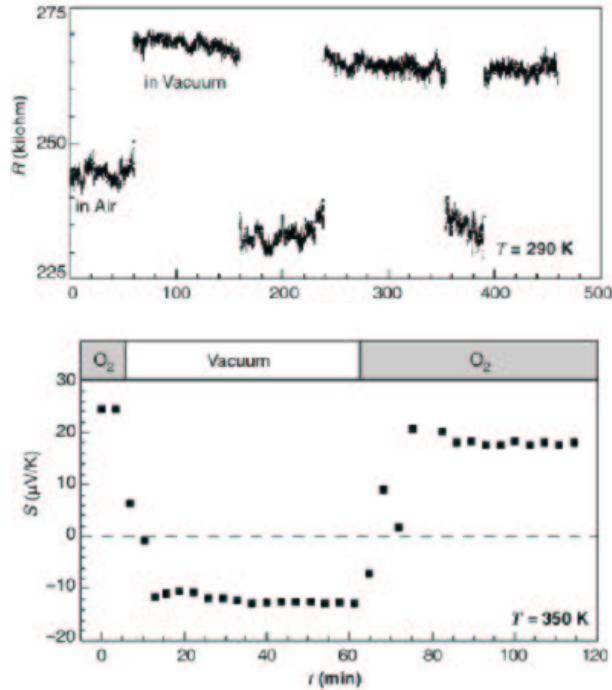illumination, while P3HT FET shows the doping effect with oxygen expo-
sure.

Figure 7.3: Upper: The single-wall carbon nanotube shows reducing resistance when exposing to O_2. Lower: The carrier species are alternatively n-type and p-type for vacuum and O_2-exposure[56].

single-wall carbon nanotubes and its resultant modulation in the electronic properties[46, 56, 57, 61]. Fig. 7.3 shows the modulation in electronic properties due to such O_2 exposure. It appears that the resistance of the nanotubes is reduced to some extent for air exposure. Moreover the resistance shows a reversible increase when the nanotubes are placed in vacuum again. In addition, the carrier specie of the nanotubes changes from n-type to p-type when the nanotubes are exposed to air, and this process can be reversibly repeated.

Jhi *et al.*[46] first give a theoretical account for such modulation due to oxygen exposure. Due to the reversibility, they regard the p-doping as a consequence of physically adsorbed oxygen molecule. By carrying out a first principle calculation, they found that the intermolecular interaction between O_2 and carbon nanotube has a potential of depth about few hundreds of meV. They also calculate the band structure for the oxygenated single-wall carbon nanotube in which each unit cell contains one oxygen molecule. As shown
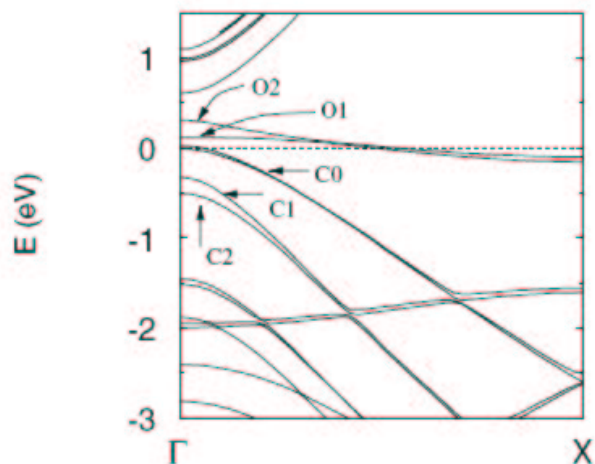
69

Figure 7.4: The band structure for single-wall carbon nanotube in which each unit cell contains one oxygen molecule. Based on the spin unpolarized calculation, the Fermi level now is slightly below the host valence band, and it indicates that the oxygenated material is a metal now.

in Fig. 7.4, the band structure contains two additional half-filled bands contributed from the adsorbed O_2. Most importantly, the Fermi level lies within the valence band such that there are free holes which are delocalized through the whole tube at zero temperature, i.e. the oxygenated carbon nanotube becomes a metal. This transformation from a intrinsic semiconductor to metal, suggested by the band structure, is valid to explain the p-doping effect by O_2.

The band structure can be viewed as a set of bands from carbon weakly interacting with the O_2 orbitals. As can be seen in Fig. 7.4, the degenerate band associated with degenerate oxygen orbitals, labeled by O1 and O2, are split due to the fact that the two oxygen orbitals have different symmetry when coupling with the carbon atoms. Similarly, the bands labeled by C1 and C2, which are degenerate in the absence of such hybridization, are also split due to different category of symmetry. Therefore the band C2 and O2 have wave functions which are mixed with carbon and oxygen atomic orbitals. This can be seen in Fig. 7.5, (a) stands for the bonding combination of the mixing for C2 which yields a lower energy, while (b) is the anti-bonding combination for band O2. However, the band labeled by C0 is orthogonal to
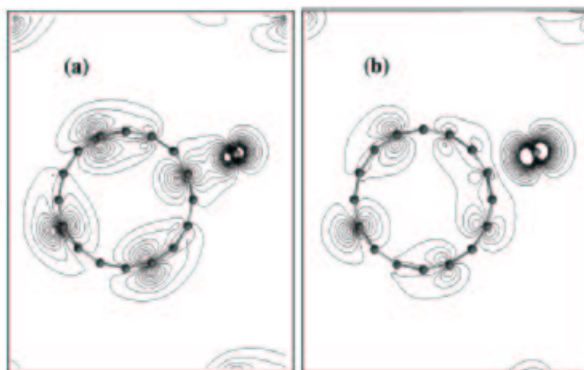
70

Figure 7.5: The wave function contour for the band states labeled by O2 (b) and C2 (a) in Fig. 7.4.

the oxygen orbitals and thus free of such split.

7.3 Electronic structure for oxygenated poly-thiophene

The chemical structure for a thiophene is shown in the upper panel in Fig. 7.6. A thiophene contains six π-electrons, four of which from carbon atoms and the rest from the sulfur atom. The π-band shown in the left panel of Fig. 7.7 is obtained from the set of tight-binding parameters given by ε_1=-1 eV, ε_2=0, ε_s=-3.8 eV, t_1=-2.8 eV, t_2=-3.5 eV, t_3=-2.5 eV, and τ=-3.2 eV[62]. The Fermi level is set at zero. The HOMO level corresponds to the edge state labeled by C_{π^*} of the valence band (VB). For states near the HOMO level, their wave functions have most components on the two top carbon atoms with an anti-bonding combination. The two flat parts labeled by S0 and S1 have most components on the sulfur atom.

The magnitude of τ, a measure of π-delocalization between molecular orbitals on adjacent thiophene units, can alter the position of HOMO level. As $|\tau|$ increases, the bandwidth of VB increases and hence the HOMO level is elevated. The chemical structure for P3HT causes it to have more planar conformation than PTT since in the latter there are more side-chain repulsions[60]. Therefore larger magnitude of τ can be expected in P3HT. Consequently the right panel in Fig. 7.7 demonstrates the lowering of HOMO level and the reduction of the bandwidth of VB for the identical tight-binding
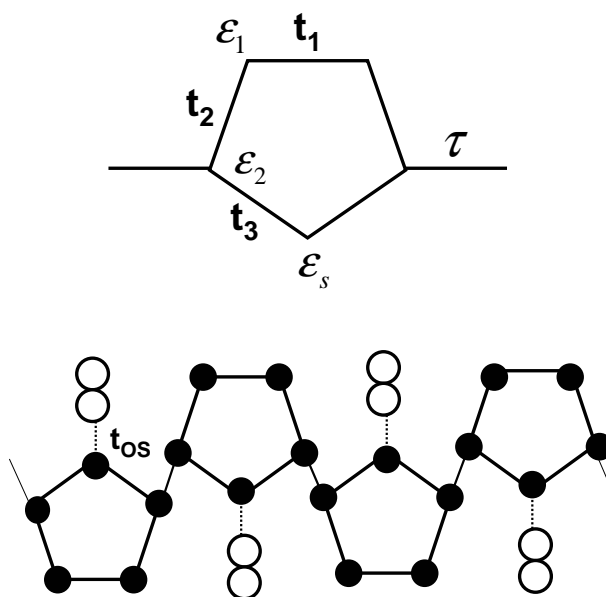
71

Figure 7.6: The upper panel shows the chemical structure for polythiophene and its tight-binding parameters for the π-band. The lower panel represents the configuration for the combined system for polythiophene containing the adsorbed O_2 (empty circles).
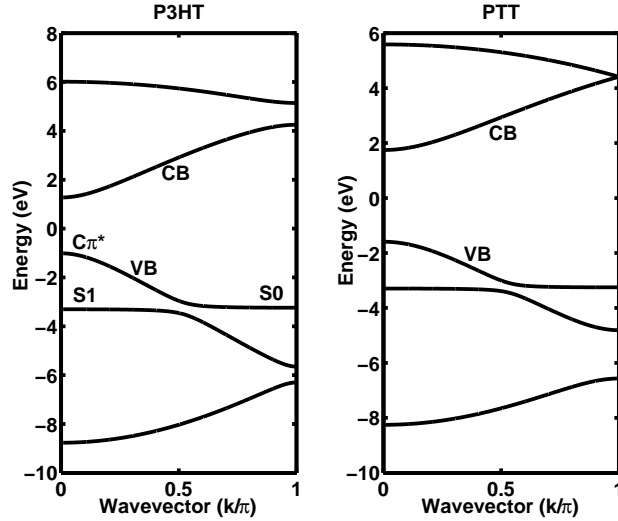
Figure 7.7: The π-bands for polythiophene with the Fermi level is set at energy zero. The band resulting from larger $|\tau|$ in the left panel shows elevated HOMO level and wider valence bandwith in comparison to the band with smaller $|\tau|$ in the right panel. We identify the left π-band with P3HT while the right with PTT. In fact the IPs are 4.98 and 5.22, respectively, for P3HT and PTT[60].

parameters except τ of -2.2 eV. We identify the left π-bands with P3HT while the right with PTT. The great difference in air stability of these two polymers will be discussed below in order to illustrate the essence of dark doping by O_2.

The donor site which interacts with O_2 is the sulfur atom in thiophene because the heteroatom contains a lone pair of electrons[63]. Consequently we consider the configuration in the lower panel of Fig. 7.6 to represent the combined system for polythiophene and O_2. Besides, we consider the case in which each thiophene unit is attached by one O_2 to simulate the situation for high density adsorption. Note that the wave functions for the π-band are composed of p_z atmoic orbitals as we regard the plane for thiophene as the x-y plane. The π-band wave functions have the odd inversion symmetry with respect to the thiophene plane. On the other hand, taking the O_2 bond as y-axis the O_2 molecule has its two valence electrons occupying the two degenerate molecular orbitals π_x^* and π_z^*. According to the adsorption configuration in Fig. 7.6, only the π_z^* has nonvanishing coupling with the π-band of the host material due to symmetry. Now we can regard the combined system as a thiophene chain weakly interacting a O_2 chain. As in the case of

single-wall carbon nanotube[46], the combined system here is going to have an additional half-filled band associated with the π_z^* oxygen orbital.

In an isolated O_2, the spins of the two electrons in the π_z^* and π_x^* orbitals are in triplet configuration due to the strong Coulomb correlation. However once the density of the adsorbed O_2 is so high that an O_2 band form through hybridization with the polymer π-bands, the oxygen wave functions become delocalized Bloch state and the spin correlation is no longer important. We can then treat the highly oxygenated polymer in a spin-independent fashion and ignore the exchange interaction. Such theoretical approach has been shown to be valid for carbon nanotube[46, 61]. Because of the hybridization, the expectation value of the electron occupation in each O_2 is no longer fixed at 2 as in the isolated molecule. The O_2 on-site energy depends on the occupation number due to Coulomb repulsion. The repulsion can be simplified if we use a mean-field description, that is

$$U a_\uparrow^\dagger a_\uparrow a_\downarrow^\dagger a_\downarrow \longrightarrow U a_\uparrow^\dagger a_\uparrow < n_\downarrow > + U < n_\uparrow > a_\downarrow^\dagger a_\downarrow \tag{7.1}$$

Therefore we define the on-site energy for π_z^* orbital of spin σ as

$$\varepsilon_\sigma = \xi + U \langle n_{-\sigma} \rangle, \tag{7.2}$$

where $n_{-\sigma}$ represents the occupation operator for electron of opposite spin on the same orbital[64]. $\langle \rangle$ is the ground state expectation value. Hence the actual on-site energy has to be determined self-consistently if additional electrons occupying the orbital. For later convenience we define the on-site energy for free oxygen band as $\varepsilon_0 \equiv \xi + U/2$, which corresponds to a level below vacuum by 5.8 eV.

The band structure of the combined system is made up with an almost flat oxygen band and a set of π-bands from the thiophene chain. The weak hybridization between the oxygen π_z^* and sulfur atomic orbitals here can split the bands from its unperturbed ones and allow electrons transferring to O_2. The ultimate band structure, with consideration of the correlation effects, is obtained as follows. We first consider the case of P3HT. When P3HT is isolated from the O_2 chain, the top of valence band lies above the oxygen band because P3HT has an IP of 5 eV while the oxygen band lies below vacuum by 5.8 eV as indicated by ε_0 in Fig. 7.8. Once the coupling t_{OS} is turned on, the electrons occupying the top of valence band may transfer to the lower oxygen band, which cause a lift of oxygen band according to Eq. (7.2) as shown by the arrow in Fig. 7.8. The positions of Fermi level and the flat oxygen band, which depends on the occupance on π_z^*, have to be determined in a self-consistent manner. Here we take advantage of the narrowness of the oxygen band to have a simpler way determining both positions. Since
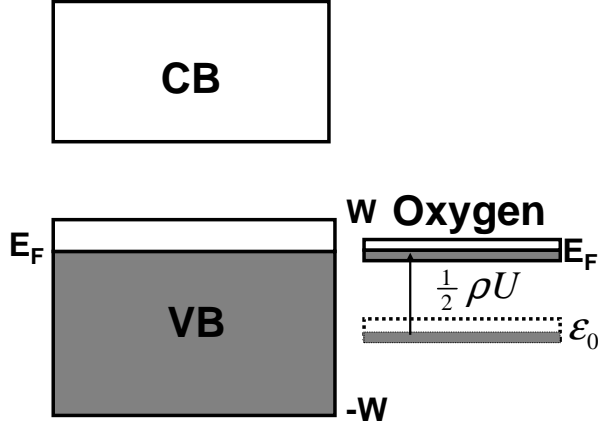
Figure 7.8: Schematic plot for valence and conduction bands for organic semiconductor. Due to electron transferred to O_2, the oxygen band is shifted upward as a result of increasing Coulomb repulsion.

the flat oxygen band can neither be empty nor filled because O_2 has a large IP and a small EA, Fermi level must be pinned with the flat band in order to keep the π_z^* having an occupation not far from unity on average, i.e. a nearly half-filled oxygen band. If we neglect the perturbation due to the weak coupling t_{OS}, the position of the flat band is solely determined by the π_z^* on-site energy. Thus the Fermi level can be given by a simple relation

$$E_F = \varepsilon_0 + \frac{\rho}{2}U , \qquad (7.3)$$

where ρ is the density of electron transferred to O_2. On the other hand, the transferred electron, which lift the oxygen band as shown in Fig. 7.8, has to coincide with the total number of empty states between the valence band edge and Fermi level. If we set the center of valence band as reference and approximate its dispersion as $\epsilon(k) = W \cos k$, then the transferred electron density is given by

$$\rho = \frac{2}{\pi} \cos^{-1}(\frac{E_F}{W}) . \qquad (7.4)$$

As shown in Fig. 7.9, ρ can be obtained by solving Eq. (7.3) and (7.4) with the given dimensionless on-site energy ε_0/W and Coulomb repulsion U/W. As shown in Fig. 7.10, as long as the HOMO level, or the top of valence band, lies above the center of free oxygen band ε_0, the density of transferred
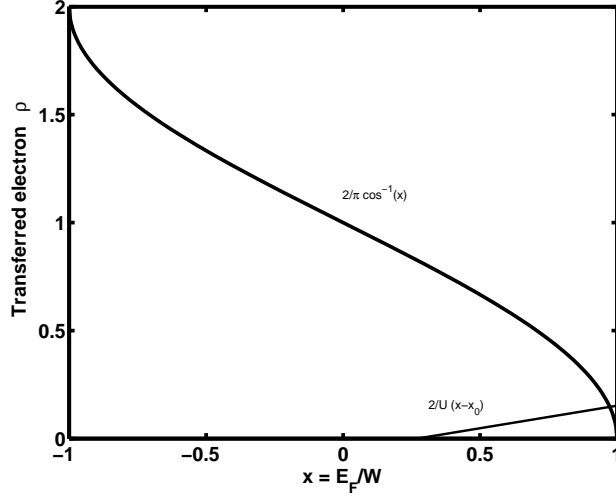
Figure 7.9: Plot for solving Eq. (7.3) and Eq. (7.4).

electron ρ is nonzero. We shall note that the transferred electron ρ obtained by the above scheme may be slightly overestimated under the approximation of cosine dispersion for valence band.

7.4 The p-doping in the condition of dark and illumination

Below we discuss the band structure of the oxygenated polymer calculated by self-consistent tight-binding method. The weak coupling t_{OS} perturbs the bands more significantly which have larger components on sulfur and oxygen atoms. Therefore, the oxygen band and the segments S0 and S1 are mixed with nonzero t_{OS}. The value of t_{OS} can actually by the integral $\frac{1}{4\pi\epsilon} \int d^3\mathbf{r}\varphi(\mathbf{r})\frac{1}{r}\phi(|\mathbf{r}-\mathbf{d}|)$, where the wave functions φ and ϕ, respectively, stand for the p_z orbitals on sulfur and oxygen atoms in Fig. 7.6. d is the separation between them and it can be determined by estimating the adsorption potential with Lennard-Jones 6-12 form in which the attraction part is assumed to be a universal function of polymer band gap for all carbon backbone based on sp^2 bonding in previous chapter. In this way we have t_{OS}=0.2 eV.

The resultant π-band structure is shown in the left panel of Fig. 7.11 with the transferred electron density ρ=0.15 for the oxygenated P3HT in Fig. 7.6. The parameters ε_0/W and U/W are, respectively, 0.27 and 9.6 and Fermi level E_F/W=0.97 lies just below the edge of valence band. Hence the
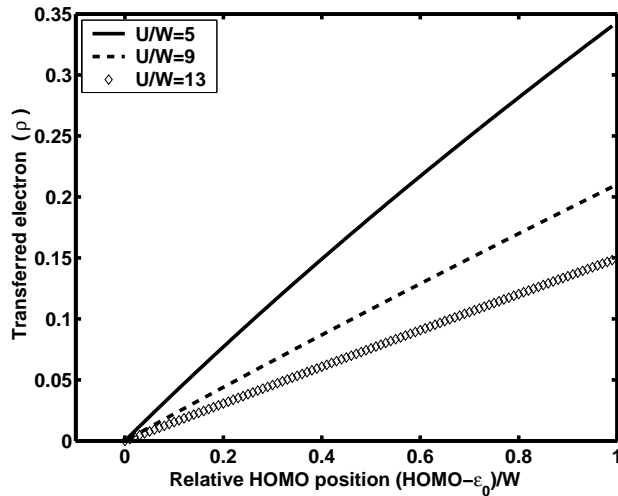
Figure 7.10: The relation between the transferred electron ρ per unit cell and the position of host HOMO level.
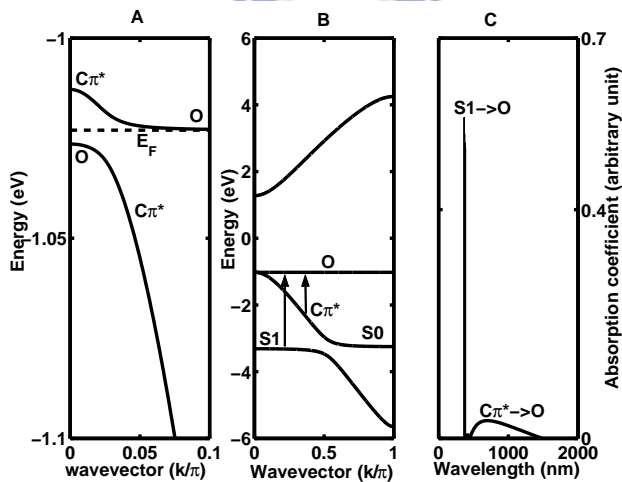

Figure 7.11: A: Partial band structure near the Fermi level (dashed line) for oxygenated P3HT. The free holes occupy the states labeled by C_{π^*}. B: The oxygen band is degenerate with the valence band edge. C: Absorption due to photon excitation in the oxygenated P3HT.
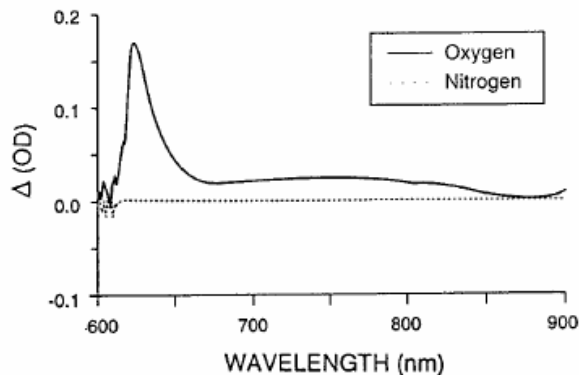
Figure 7.12: The absorption difference for O_2-exposure and N_2-exposure P3HT.

oxygenated P3HT is a metal where free hole carriers exist. Despite of the hybridization with O_2, the wave functions of C_{π^*} valence band edge still have the dominate contribution from carbon p_z orbital. The nature of the holes is this identical with the holes on a pristine polymer without oxygen. On the other hand, holes in the oxygen band can hardly move due to the very large effective mass. This is consistent with the experimental finding that the average hole mobility is decreased by the oxygenation. This transformation from intrinsic semiconductor to metal by adsorbed O_2 explains the effect of O_2 p-doping in dark condition. Note that such doping occurs even at zero temperature, in contrast to the n/p doping for inorganic semiconductors where thermal energy is required to lift the carriers to the bands. Moreover, O_2 act collectively instead of giving its own hole individually as in inorganic semiconductors. In addition to the empty states near C_{π^*} generate free hole carriers at ground state, photons can excite the electrons in the sulfur band and the valence band to the empty parts of the oxygen band. Since only the sulfur atom has significant optical transition matrix element with oxygen atom, the absorption coefficient is proportional to the sulfur component of the initial Bloch state and the optical joint density of state. The relative absorption spectrum is shown in the right panel of Fig. 7.11. The sharp peak at 2.3 eV (400 nm) is from the sulfur band, while the broad tail is from the valence band. This result is remarkably consistent with the experiment[53].

Reducing the magnitude of τ can lower the HOMO position and alter the p-doping significantly. For polythiophene with IP larger than 5.8 eV due to smaller $|\tau|$ as the case of PTT in Fig. 7.7, the additional oxygen band will

lie close the the edge of valence band in the band gap. The p-doping in dark is significantly suppressed by the large IP, but a photoinduced p-doping is possible. Obviously we can generalized the oxygen doping dependence on IP to other organic semiconductors. For small molecules such as pentacene with IP of 6 eV[37], the off-current for pentacene FET is apparent only under both illumination and O_2 exposure[55], in complete agreement with our prediction.

We would also like to remark further on the relation between the adsorption density and the p-doping. It seems that a single O_2 is not able to reconcile the picture for such p-doping because of its low EA. Consider the case of weak coupling for the single O_2 and assume the organic semiconductor were indeed p-doped by it, the Fermi level of the combined system would go down and touch the edge of valence band in order to generate one free hole. Once this took place, the lost electron would occupy nowhere but the O_2, which however took exceedingly high energy as indicated by the small EA. Therefore a cluster of adsorbed O_2, as in the lower panel of Fig. 7.6, is required to accept the additional electron. The free hole carrier density has been quantitatively extracted from the pinch-off voltage of P3HT FET[54]. It can be seen that the carrier density actually rises only after a sufficiently long time of O_2 exposure, say 1 hour. This observation supports that doping in the dark has a threshold adsorption density for the cluster formation.

Adsorption of O_2 seems to be universal among the organic semiconductor based on the sp^2-bonding carbon backbone, such as polythiophene, carbon nanotube, pentacene, and emissive materials for organic light-emitting diodes. The O_2 adsorption has other effects on the electronic properties in addition to the p-doping. For organic semiconductors with defects, the O_2 can worsen the transport for electron by forming a hybridized state with the electron trap, which will bind the electron more tightly. Under such circumstance, the electron mobility can be much smaller than the hole mobility, which is usually observed for a large class of conjugated polymers and small molecules.

7.5 The Fermi level alignment in the presence of the oxygen band

In addition to the bulk properties discussed above, oxygenation is also expected to modify the metal interface dramatically. The fact that the Fermi level is pinned by the flat oxygen band is of crucial importance when the organic material is in contact with metal. Naively, the Fermi level is fixed by the metal and can be anywhere within the band gap. However, for the oxy-
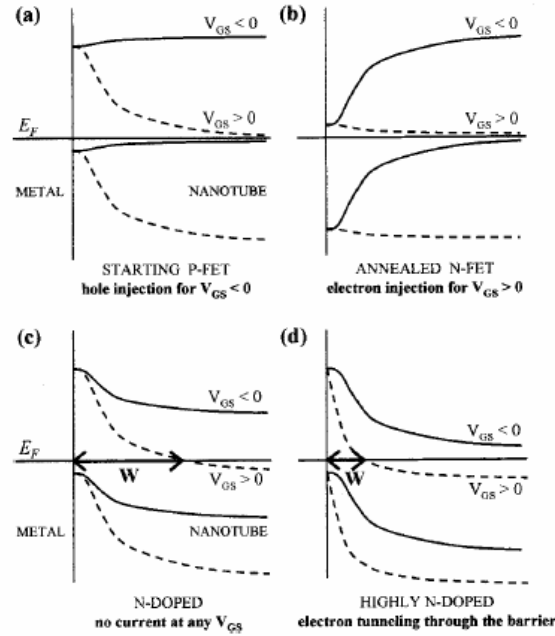
Figure 7.13: Band alignment in single-wall carbon nanotube[57].

genated organic semiconductors, the adsorbed oxygen molecules contribute a band within the band gap which pin the Fermi level of the metal by its high unoccupied density of state. As can be seen in Fig. 7.13, different barrier heights are found for exposed and unexposed carbon nanotube FET's[57].

Recently an ultraviolet photoelectron spectroscopy study of the titanyl phthalocyanine (TiOPc) thin film also supports the concept of bulk p-doping[58]. It was found that the exposed organic material could have enough free hole carriers in bulk region such that a reverse band bending, in contrast to the unexposed film, is formed at the interface. Moreover, as can be seen in Fig. 7.14 for the case of TiOPc, the fact that the Fermi level is fixed about 0.6 eV above the HOMO level for various metal contacts[58].

7.6 Concluding remark

Compared with metals and insulators, semiconductors are unique in that their electrical properties can be widely tuned by the dopants. Inorganic semiconductors are usually classified into intrinsic and extrinsic ones depending on the existence of the dopants, and analogy has been made to or-
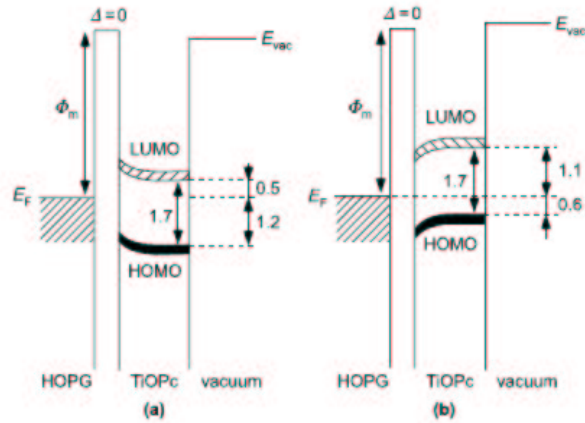
80

Figure 7.14: Band alignment between TiOPc and various metal contacts[58].

ganic semiconductors. Most of the materials used in organic semiconductor devices are thought to be intrinsic, since no dopant is intentionally incorporated. Yet it is well known that their electrical conductivity is highly sensitive to external conditions despite the materials has been carefully purified. The distinction between intrinsic and extrinsic semiconductors is therefore blurred and questionable. In the past several years it became clear that the gas molecules are responsible for such sensitivity. In particular, the ubiquitous molecular oxygen physically adsorbed to the organic semiconductors is shown to cause a p-doping, in sharp contrast to inorganic semiconductors where doping is through chemical bonding with impurity atoms. So far very little is known about the nature of oxygen doping, and apparently the well-established donor/acceptor doping theory of inorganic semiconductor is far from applicable[65].

Bibliography

[1] G. Dehlinger, L. Diehl, U. Gennser, H. Sigg, J. Faist, K. Ensslin, D. Grützmacher, and E. Müller, Science **290**, 2277 (2000).

[2] S. Kumar, B. S. Williams, S. Kohen, Q. Hu, and J. L. Reno, Appl. Phys. Lett. **84**, 2494 (2004).

[3] B. S. Williams, S. Kumar, Q. Hu, and J. L. Reno, Electronics Letters **40**, 431 (2004).

[4] O. Bonno, J. L. Thobel, and F. Dessenne, Physica E **33**, 13 (2006).

[5] F. Bloch, Z. Phys. **52**, 555 (1928).

[6] C. Zener, Proc. R. Soc. London A, **145**, 523 (1934).

[7] E. E. Mendez, F. Agulló-Rueda, J. M. Hong, Phys. Rev. Lett. **60**, 2426 (1988).

[8] Y. Shimada, K. Hirakawa, M. Odnoblioudov, and K. A. Chao, Phys. Rev. Lett. **90**, 046806 (2003).

[9] N. Seiken and K. Hirakawa, Phys. Rev. Lett. **94**, 057408 (2005).

[10] M.A. Odnoblyudov, I.N. Yassievich, M.S. Kagan, Yu.M. Galperin, and K.A. Chao, Phys. Rev. Lett. **83**, 644 (1999).

[11] M. A. Odnoblyudov, I. N. Yassievich, V. M. Chistyakov, and K. A. Chao, Phys. Rev. B **62**, 2486 (2000); M. A. Odnoblyudov, A. A. Prokofiev, I. N. Yassievich, and K. A. Chao, Phys. Rev. B **70**, 115209 (2004).

[12] I. V. Altukhov, E. G. Chirkova, V. P. Sinis, M. S. Kagan, Yu. P. Gousev, S. G. Thomas, K. L. Wang, M. A. Odnoblyudov, and I.N. Yassievich, Appl. Phys. Lett. **79**, 3909 (2001)

[13] M. S. Kagan and I. N. Yassievich, Physica E **13**, 916 (2002).

[14] S. M. Sze, *Physics of Semiconductor Devices* (John Wiley and Sons, New York, 1981).

[15] J. M. Luttinger and W. Kohn, Phys. Rev. **97**, 869 (1955).

[16] G. L. Bir and G. E. Pikus, *Symmtery and Strain Effects in semiconductors* (Wiley, New York, 1974).

[17] C. G. Van de Walle, Phys. Rev. B **39** 1871 (1989).

[18] C. G. Van de Walle and R. M. Martin, Phys. Rev. B **34** 5621 (1986).

[19] A. Blom, M. A. Odnoblyudov, I. N. Yassievich, and K. A. Chao, Phys. Rev. B **65**, 155302 (2002).

[20] P. Lawaetz, Phys. Rev. B **4**, 3460 (1971).

[21] K. Tomizawa, *Numerical Simulation of Submicron Semiconductor Devices* (Artech House, Boston, 1993).

[22] A. A. Andronov, Sov. Phys. Semicond. **21**, 701 (1987).

[23] S. Datta, *Quantum Phenomena* (Addison-Wesley, New York, 1989).

[24] V. N. Abakumov, V. I. Perer, and I. N. Yassievich, *Nonradiative Recombination in Semiconductors*, edited by V. M. Agranovich and A. A. Maradudin, Modern Problems in Condensed Matter Sciences, Vol.33 (North Holland, Amsterdam, 1991).

[25] W. Quade, G. Hupper, E. Schöll, and T. Kuhn, Phys. Rev. B **49**, 13408 (1994).

[26] E. Schöll, *Nonequilibrium Phase Transitions in Semiconductors*(Springer,Berlin,1987).

[27] R. H. Friend *et al.*, Nature

[28] J. P. Lowe, *Quantum Chemistry* (Academic Press, New York, 1993).

[29] C. R. Fincher, Jr. D. L. Peebles, A. J. Hegger, M. A. Druy, Y. Matsumura, A. G. MacDiarmid, H. Shirakawa, and S. Ikeda, Solid State Commun. **27**, 489 (1979).

[30] W. P. Su, J. Schrieffer, and A. Hegger, Phys. Rev. B **22**, 2099 (1980).

[31] H. F. Meng and T. M. Horng, Physica B **304**, 119 (2001).

[32] D. K. Campbell, A. R. Bishop, and K. Fesser, Phys. Rev. B **26**, 6862 (1982).

[33] M. Rohlfing and S. G. Louie, Phys. Rev. Lett. **99**, 1954 (1999).

[34] P. Gomes da Costa, R. G. Dandrea, and E. M. Conwell, Phys. Rev. B **47**, 1800 (1993).

[35] J. Pflaum *et al.*, Chem. Phys. **325**, 152 (2006).

[36] L. Bozano *et al.*, Appl. Phys. Lett. **74**, 1132 (1999).

[37] T. Yasuda *et al.*, Appl. Phys. Lett. **85**, 2098 (2004).

[38] P. W. M. Blom and M. J. M. de Jong, IEEE J. Sel. Top. Quant. **4**, 105 (1998).

[39] M. J. Tsai and H. F. Meng, J. Appl. Phys. **97**, 114502 (2005).

[40] H. F. Meng and Y. S. Chen, Phys. Rev. B **70**, 115208 (2004).

[41] D. A. dos Santōs and J. L. Brédas, Synth. Met. **101**, 486 (1999).

[42] *Handbook of Photochemistry and Photobiology*, Chapter 11, edited by H.S. Nalwa, Volume 2: Organic Photochemistry (American Scientific Publishers, 2003).

[43] N. W. Aschroft and N. D. Mermin, *Solid State Physics* (Harcourt Brace College Publisher, New York, 1976).

[44] J. J. Sakurai, *Modern Quantum Mechanics* (Addison-Wesley, New York, 1994).

[45] J. C. Slater, *The Calculation of Molecular Orbitals* (Wiley-Interscience, New York, 1979).

[46] S. H. Jhi, S. G. Louie, and M. L. Cohen, Phys. Rev. Lett. **85**, 1710 (2000).

[47] *CRC Handbook of Chemistry and Physics*, 79th ed., edited by D. R. Lide (CRC, Boca Raton, FL, 1998).

[48] K. Kažukauskas *et al.*, Appl. Phys. Lett. **80**, 2017 (2002).

[49] I. H. Campbell and D. L. Smith, Physics of organic electronic devices in *Solid State Physics* **55** (Acadmeic Press, New York, 2001).

[50] P. Stallinga *et al.*, Synth. Met. **111**, 535 (2000).

[51] H. Fong *et al.*, Jpn. J. Appl. Phys. **41**, L1122 (2002).

[52] R. C. Haddon *et al.*, Appl. Phys. Lett. **67**, 121 (1995).

[53] M. S. A. Abdou, F. P. Orfino, Y. Son, and S. Holdcroft, J. Am. Chem. Soc. **119**, 4518 (1997).

[54] E. J. Meijer, C. Detcheverry, P. J. Baesjou, E. van Veenendaal, D. M. de Leeuw, and T. M. Klapwijk, J. Appl. Phys. **93**, 4831 (2003).

[55] S. Ogawa, T. Naijo, Y. Kimura, H. Ishii, and M. Niwano, Jpn. J. Appl. Phys. **45**, 530 (2006).

[56] P. G. Collins, K. Bradley, M. Ishigami, and A. Zettl, Science **287**, 1801 (2000).

[57] V. Derycke, R. Martel, J. Appenzeller, and Ph. Avouris, Appl. Phys. Lett. **80**, 2773 (2002)

[58] T. Nishi, K. Kanai, Y. Ouchi, M. R. Willis, K. Seki, Chem. Phys. **325**, 121 (2006).

[59] R. G. Tonkyn, J. W. Winniczek, and M. G. White, Chem. Phys. Lett. **164**, 137 (1989).

[60] B. Ong, Y. Wu, L. Jiang, P. Liu, and K. Murti, Synt. Met. **142**, 49 (2004).

[61] S. Dag, O. Gülseren, T. Yildirim, and S. Ciraci, Phys. Rev. B **67**, 165424 (2003).

[62] *Organic Electronic Materials, Conjugated Polymers and Low Molecular Weight Organic Solids*, edited by R. Farchioni and G. Grosso (Springer, Berlin, 2001).

[63] *Handbook of Photochemistry and Photobiology*, edited by H. S. Nalwa, Volume 2: Organic Photochemistry (American Scientific Publishers, 2003).

[64] J. R. Schrieffer, J. Vac. Sci. Tech. **9**, 561 (1971).

[65] B. A. Gregg, S. G. Chen, and R. A. Cormier, Chem. Mater. **16**, 4586 (2004).